

Mechanism of exotic density-wave and beyond-Migdal unconventional superconductivity in kagome metal AV_3Sb_5 (A=K, Rb, Cs)

Rina Tazai*, Youichi Yamakawa, Seiichiro Onari, and Hiroshi Kontani*

Department of Physics, Nagoya University, Furo-cho, Nagoya 464-8602, Japan.

(Dated: April 26, 2022)

Exotic quantum phase transitions in metals, such as the electronic nematic state, have been discovered one after another and found to be universal now. The emergence of unconventional density wave (DW) order in frustrated kagome metal AV_3Sb_5 and its interplay with exotic superconductivity attract increasing attention. We find that the DW in kagome metal is the bond-order, because the sizable inter-site attraction is caused by the quantum interference among paramagnons. This mechanism is significant in kagome metals since the geometrical frustration prohibits the freezing of paramagnons. In addition, we uncover that moderate bond-order fluctuations mediate sizable pairing glue, and this mechanism gives rise to both singlet s -wave and triplet p -wave superconductivity. Furthermore, characteristic pressure-induced phase transitions in CsV_3C_b are naturally understood by the present theory. Thus, both the exotic density wave and the superconductivity in geometrically frustrated kagome metals are uniquely explained by the quantum interference mechanism.

*Corresponding author. Email: tazai@s.phys.nagoya-u.ac.jp (R.T.); kon@slab.phys.nagoya-u.ac.jp (H.K.)

Teaser: The exotic density wave, superconductivity and their interplay in novel kagome metals are revealed based on the quantum interference mechanism.

INTRODUCTION

Rich quantum phase transitions in strongly correlated metals with multiple degrees of freedom and geometrical frustration have been discovered one after another recently [1–4]. To understand such rich phase transitions, a significant ingredient is various quantum interference processes among different fluctuations [5–12]. The recent discovery of unconventional density-wave (DW) order and exotic superconductivity in kagome lattice metal AV_3Sb_5 (A=K, Rb, Cs) have triggered enormous number of experimental [13–22] and theoretical [23–28] researches. Especially, the nontrivial interplay between density-wave and superconductivity in highly frustrated kagome metals has attracted increasing attention in condensed matter physics.

At ambient pressure, AV_3Sb_5 exhibits charge-channel DW order at $T_{\text{DW}} = 78, 94$ and 102 K for A=K, Cs and Rb, respectively [13, 14, 29, 30]. Below T_{DW} , 2×2 (inverse) star of David pattern was observed by STM studies [31, 32]. The absence of acoustic phonon anomaly at T_{DW} [33] would exclude DW states due to strong electron-phonon coupling. As possible electron-correlation-driven DW orders, charge/bond and loop-current (LC) orders [23, 25, 28, 34–36] have been proposed theoretically, mainly based on the extended Hubbard model with the on-site (U) and the nearest-neighbor site (V) Coulomb interactions. However, when $V \ll U$ due to Thomas-

Fermi screening, previous studies predicted strong magnetic instability, in contrast to the small spin fluctuations in AV_3Sb_5 at T_{DW} [29, 30, 37].

Below T_{DW} , exotic superconductivity occurs at $T_c = 1 \sim 3$ K at ambient pressure [18, 19]. The finite Hebel-Slichter peak in $1/T_1T$ [29] and the absence of the impurity bound-state below T_c [38] indicate the singlet s -wave superconducting (SC) state. On the other hand, the possibilities of triplet pairing state [39] and nematic SC state [40, 41] have been reported. In addition, topological states have been discussed intensively [42]. Under pressure, T_{DW} decreases and vanishes at the DW quantum critical point (DW-QCP) at $P \sim 2$ GPa. For A=Cs, T_c exhibits a nontrivial double SC dome in the DW phase, and the highest T_c ($\lesssim 10$ K) is realized at the DW-QCP [15]. In addition, theoretical phonon-mediated s -wave T_c is too low to explain experiments [24]. Thus, non-phonon SC state due to DW fluctuations [43] is naturally expected in AV_3Sb_5 .

The current central issues would be summarized as: (i) Origin of the DW state and its driving mechanism, (ii) Mechanism of non-phonon SC state, and (iii) Interplay between DW and superconductivity. Such nontrivial phase transitions would be naturally explained in terms of the quantum interference mechanism. The interference among spin fluctuations [5, 6, 9, 10, 44, 45] (at wavevectors \mathbf{q} and \mathbf{q}') give rise to unconventional DW at $\mathbf{q} + \mathbf{q}'$, which is shown in Fig. 1 (a). This mechanism has

been applied to explain the orbital/bond-orders in various metals [4, 46–49]. It is meaningful to investigate the role of the paramagnon interference in kagome metals because the geometrical frustration prohibits the freezing of paramagnons. Its lattice structure, band dispersion, and Fermi surface (FS) with three van Hove singularity (vHS) points are shown in Figs. 1 (b), (c) and (d), respectively.

In this paper, we present a unified explanation for the DW order and exotic SC state in geometrically frustrated kagome metal AV_3Sb_5 that is away from the magnetic criticality, by focusing on the beyond-mean-field electron correlations. The DW is identified as the “inter-sublattice bond-order” that preserves the time-reversal-symmetry. It originates from the paramagnon interference mechanism that provides sizable inter-sublattice backward and umklapp scattering. In addition, we uncover that the smectic DW fluctuations induce sizable “beyond-Migdal” pairing interaction that leads to the singlet s -wave SC state. The triplet p -wave state also appears when spin and DW fluctuations coexist. The origins of the star of David order, the exotic superconductivity, and the strong interplay among them are uniquely explained based on the quantum interference mechanism. This mechanism has been overlooked previously.

In the discussion section, we study the P - T phase diagram and the impurity effect on the SC states. The commensurate-incommensurate (C-IC) DW transition is obtained at 1GPa based on the realistic model constructed by the first-principles study. Based on this C-IC transition scenario, we put the following theoretical predictions (i)-(iv): (i) For $0 \leq P < 1\text{GPa}$, the commensurate DW emerges. (ii) For $P > 1\text{GPa}$, the DW state turns to be incommensurate due to the pressure-induced self-doping on the b_{3g} -orbital FS (about 1.5 %). (iii) As the highest- T_c dome at $P \sim 2\text{GPa}$, anisotropic s -wave SC state is realized by the bond-order fluctuations. (iv) In another SC dome at $P \sim 0.7\text{GPa}$, both s - and p -wave states can emerge since the spin and bond-order fluctuations would be comparable. Thus, impurity-induced p -wave to s -wave transition may occur. The present key findings will stimulate future experiments on AV_3Sb_5 .

RESULTS

Bandstructure with three vHS points

We analyze the following six orbital kagome lattice Hubbard model introduced in Ref. [25]. It is composed of three b_{3g} -orbitals (A, B, C) and three b_{2g} -orbitals (A', B', C'). Orbitals A and A' are located at A site, for instance. The kinetic term in \mathbf{k} -space is given as

$$H_0 = \sum_{\mathbf{k}, l, m, \sigma} \epsilon_{lm}(\mathbf{k}) c_{\mathbf{k}, l, \sigma}^\dagger c_{\mathbf{k}, m, \sigma}, \quad (1)$$

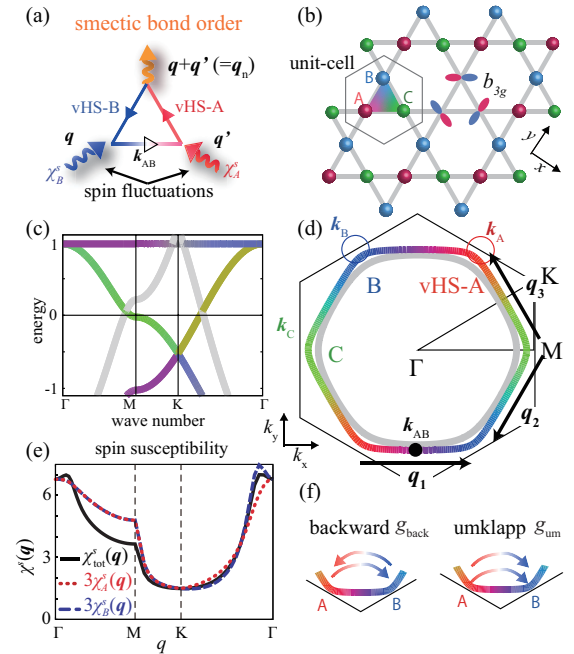


FIG. 1: **Interference mechanism, FS and three vHS points in kagome model:** (a) Smectic order at wavevector $\mathbf{q}_n = \mathbf{q} + \mathbf{q}'$ driven by the paramagnon interference mechanism. (b) Kagome lattice structure of the vanadium-plane. Three b_{3g} -orbitals A, B, C (and three b_{2g} -orbitals A', B', C') are located at A, B, C sites, respectively. (c) Band structure and (d) FSs at $n = 3.8$. The outer (inner) FS are composed of b_{3g} - (b_{2g} -) orbitals. Three vHS points \mathbf{k}_A , \mathbf{k}_B and \mathbf{k}_C are respectively composed of A (red), B (blue), and C (green) orbitals. The inter-vHS nesting vectors \mathbf{q}_n ($n = 1, 2, 3$) are shown. All b_{2g} -orbitals are expressed as gray color. (e) $\chi_A^s(\mathbf{q})$, $\chi_B^s(\mathbf{q})$, and $\chi_{\text{tot}}^s(\mathbf{q})$ in the RPA. (f) Backward and umklapp scattering between different vHS points. These processes are caused by paramagnon interference mechanism. (See Fig. 3 for detail.)

where $l, m = A, B, C, A', B', C'$. In the paper the unit of energy (in Coulomb interaction, hopping integral, and temperature) is eV. The nearest-neighbor hopping integrals are $t_{b3g} = 0.5$, $t_{b2g} = 1$ and $t_{b3g, b2g} = 0.002$, and the on-site energies are $E_{b3g} = -0.055$ and $E_{b2g} = 2.17$ [25]. In the numerical study, it is convenient to analyze the six-orbital triangular lattice model in Fig. S1 in the Supplemental Materials (SM) A, which is completely equivalent to the kagome metal in Fig. 1 (b). In the b_{3g} -orbital band shown in Fig. 1 (d), each vHS point (A, B and C) is composed of pure orbital (A, B and C), while the point $\mathbf{k}_{AB} = (\mathbf{k}_A + \mathbf{k}_B)/2$ is composed of orbitals A and B . The present b_{3g} -orbital FS in the vicinity of three vHS points, on which the pseudogap opens below T_{DW} [50–52], well captures the observed FS [31, 53, 54].

Next, we introduce the “on-site Coulomb interaction” term H_U . It is composed of the intra- (inter-) orbital interaction U (U'), and the exchange interaction $J = (U - U')/2$. Below, we fix the ratio $J/U = 0.1$.

The 4×4 matrix expression of on-site Coulomb interaction at each site, $\hat{U}^{s(c)}$ for spin (charge) channel, is explained in the SM A. In the mean-field-level approximation, the spin instability is the most prominent because of the largest interaction U . Figure 1 (e) exhibits the intra- b_{3g} -orbital static ($\omega = 0$) spin susceptibilities $\chi_A^s(\mathbf{q}) \equiv \chi_{AA,AA}^s(\mathbf{q})$ and $\chi_{\text{tot}}^s(\mathbf{q}) = \sum_m^{A,B,C} \chi_m^s(\mathbf{q})$ in the random phase approximation (RPA) at $U = 1.26$ ($\alpha_S = 0.80$ at $T = 0.02$). In the RPA, $\hat{\chi}^s(q) = \hat{\chi}^0(q)(\hat{1} - \hat{\Gamma}^s \hat{\chi}^0(q))^{-1}$, where $\hat{\chi}^0(q)$ is the irreducible susceptibility matrix and $q \equiv (\mathbf{q}, \omega_l = 2\pi Tl)$. The spin Stoner factor α_S is the maximum eigenvalue of $\hat{\Gamma}^s \hat{\chi}^0(q)$, and magnetic order appears when $\alpha_S = 1$. Thus, intra-orbital spin susceptibility gets enhanced at $\mathbf{q} \approx \mathbf{0}$ in the present kagome model. (Note that $\chi_A^s(\mathbf{q}_1)$ is small because orbitals A and B correspond to different sites, referred to as the sublattice interference [34]. Also, $\chi_{AA,BB}^s, \chi_{A'}^s$ is much smaller than χ_A^s .)

bond-order derived from DW equation

Nonmagnetic DW orders cannot be explained in the RPA unless large nearest-neighbor Coulomb interaction V ($V > 0.5U$) exists. However, beyond-RPA nonlocal correlations, called the vertex corrections (VCs), can induce various DW orders even for $V = 0$ [5, 6, 9, 10, 44]. To consider the VCs due to the paramagnon interference in Fig. 1 (a), which causes the nematicity in Fe-based and cuprate superconductors, we employ the linearized DW equation [10, 47]:

$$\lambda_{\mathbf{q}} f_{\mathbf{q}}^L(k) = -\frac{T}{N} \sum_{p, M_1, M_2} I_{\mathbf{q}}^{L, M_1}(k, p) \times \{G(p)G(p + \mathbf{q})\}^{M_1, M_2} f_{\mathbf{q}}^{M_2}(p), \quad (2)$$

where $I_{\mathbf{q}}^{L, M}(k, p)$ is the ‘‘electron-hole pairing interaction’’, $k \equiv (\mathbf{k}, \epsilon_n)$ and $p \equiv (\mathbf{p}, \epsilon_m)$ (ϵ_n, ϵ_m are fermion Matsubara frequencies). $L \equiv (l, l')$ and M_i represent the pair of d -orbital indices A, B, C, A', B', C' . $\lambda_{\mathbf{q}}$ is the eigenvalue that represents the instability of the DW at wavevector \mathbf{q} , and $\max_{\mathbf{q}} \{\lambda_{\mathbf{q}}\}$ reaches unity at $T = T_{\text{DW}}$. $f_{\mathbf{q}}^L(k)$ is the Hermite form factor that is proportional to the particle-hole (p-h) condensation $\sum_{\sigma} \langle c_{\mathbf{k}+\mathbf{q}, l, \sigma}^{\dagger} c_{\mathbf{k}, l', \sigma} \rangle$, or equivalently, the symmetry breaking component in the self-energy.

It is important to use the appropriate kernel function $I_{\mathbf{q}}^{L, M}$, which is given as $\delta^2 \Phi_{\text{LW}} / \delta G_{l'l}(k) \delta G_{mm'}(p)$ at $\mathbf{q} = \mathbf{0}$ in the conserving approximation scheme [44, 55], where Φ_{LW} is the Luttinger-Ward function introduced in the Method section. If we apply the bare interaction to $I_{\mathbf{q}}^{L, M}$ that corresponds to RPA [55], the relation $\lambda_{\mathbf{q}} > \alpha_S$ cannot be realized when H_U is local. Thus, higher-order corrections are indispensable.

Here, we apply the one-loop approximation for Φ_{LW} [6, 44]. Then, $I_{\mathbf{q}}^{L, M}$ is composed of one single-magnon

exchange Maki-Thompson (MT) term and two double-magnon interference Aslamazov-Larkin (AL) terms. Their diagrammatic and analytic expressions are explained in the Method section. Due to the AL terms, the nonmagnetic nematic order in FeSe is naturally reproduced even if spin fluctuations are very weak [6]. The importance of AL terms was verified by the functional-renormalization-group (fRG) study with constrained-RPA, in which higher-order parquet VCs are produced in an unbiased way, for several Hubbard models [4, 7, 46]. Later, we see that the AL diagrams induce the backward and umklapp scattering shown in Fig. 1 (f), and they mediate the p-h condensation at the inter-vHS nesting vector $\mathbf{q}_1 = \mathbf{k}_B - \mathbf{k}_A$.

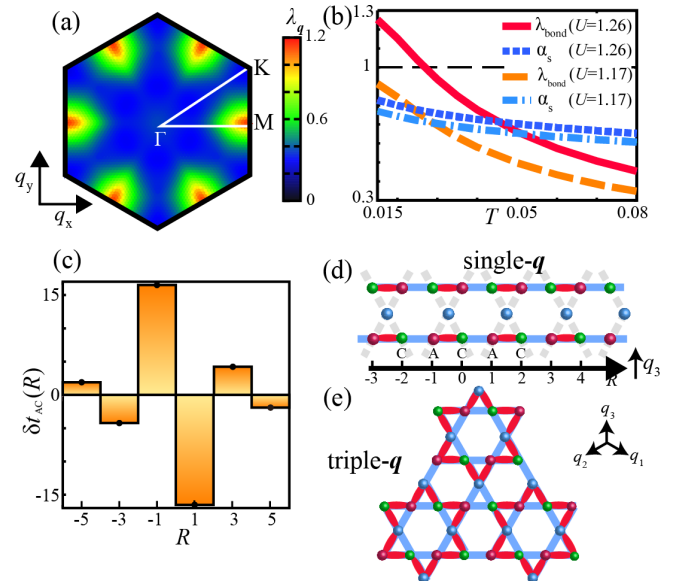


FIG. 2: **bond-order solution derived from DW equation:** (a) Obtained \mathbf{q} -dependence of the eigenvalue $\lambda_{\mathbf{q}}$ at $n = 3.8$ ($T = 0.02$ and $\alpha_S = 0.80$). $\lambda_{\mathbf{q}}$ shows peaks at \mathbf{q}_n ($n = 1, 2, 3$), consistently with experiments in AV_3Sb_5 . (b) T -dependences of λ_{bond} and α_S at $U = 1.26$ and 1.17 . The DW susceptibility ($\chi_f^c(\mathbf{q}_n) \propto 1/(1 - \lambda_{\text{bond}})$) increases as $T \rightarrow T_{\text{DW}} \approx 0.025$, whereas magnetic susceptibility ($\chi^s(\mathbf{0}) \propto 1/(1 - \alpha_S)$) is almost constant. (c) Modulation of hipping integrals $\delta t_{AC}(R a_{AC})$ for $\mathbf{q} = \mathbf{q}_3$ along the A-C direction (arbitrary unit). Its schematic picture at wavevector \mathbf{q}_3 is shown in (d). (e) Expected triple- \mathbf{q} star of David bond-order.

Figure 2 (a) exhibits the obtained \mathbf{q} -dependence of the eigenvalue $\lambda_{\mathbf{q}}$ at $n = 3.8$ ($T = 0.02$ and $\alpha_S = 0.80$). The obtained peak position at \mathbf{q}_n ($n = 1, 2, 3$) is consistent with experiments in AV_3Sb_5 . The T -dependences of $\lambda_{\text{bond}} \equiv \lambda_{\mathbf{q}_n}$ and α_S are shown in Fig. 2 (b). The DW susceptibility ($\chi_f^c(\mathbf{q}_n) \propto 1/(1 - \lambda_{\text{bond}})$) increases as $T \rightarrow T_{\text{DW}} \approx 0.025$, whereas the increment of ferromagnetic susceptibility ($\chi^s(\mathbf{0}) \propto 1/(1 - \alpha_S)$) is small. Then, what order parameter is obtained? To answer this ques-

tion, we perform the Fourier transform of the form factor:

$$\delta t_{lm}(\mathbf{r}) = \frac{1}{N} \sum_{\mathbf{k}} f_{\mathbf{q}_n}^{lm}(\mathbf{k}) e^{i\mathbf{r} \cdot \mathbf{k}}. \quad (3)$$

Then, $\delta t_{lm}(\mathbf{r}_i - \mathbf{r}_j) \cos(\mathbf{q}_n \cdot \mathbf{r}_i + \theta)$ represents the modulation of the hopping integral between \mathbf{r}_i and \mathbf{r}_j , where \mathbf{r}_i represents the center of a unit-cell i in real space, and θ is a phase factor. The bond-order preserves the time-reversal-symmetry because it satisfies the relation $\delta t_{lm}(\mathbf{r}) = \delta t_{ml}(-\mathbf{r}) = \text{real}$. (Note that the current order is $\delta t_{lm}(\mathbf{r}) = -\delta t_{ml}(-\mathbf{r}) = \text{imaginary}$.) Figure 2 (c) represents the obtained form factor $\delta t_{AC}(\mathbf{r})$ for $\mathbf{q} = \mathbf{q}_3$ along the A-C direction, where $\mathbf{r} = R\mathbf{a}_{AC}$ with odd number R . The obtained solution is a bond-order because the relation $\delta t_{CA}(\mathbf{r}) = \delta t_{AC}(-\mathbf{r})$ is verified. The relation $\delta t_{AA}(\mathbf{r}) = \delta t_{CC}(\mathbf{r}) = 0$ holds in this bond-order solution.

To summarize, we obtain the single- \mathbf{q} smectic bond-order depicted in Fig. 2 (d). In SM B, we perform the DW equation analysis for $n = 3.6$ and 3.7 and obtain very similar results to Fig. 2. Thus, the robustness of the bond-order is confirmed, irrespective of the Lifshitz transition at $n \approx 3.71$. In the triple- \mathbf{q} state, in which three bond-orders with $\mathbf{q}_1, \mathbf{q}_2, \mathbf{q}_3$ coexist, a star of David bond-order in Fig. 2 (e) appears. Figure S4 in SM C shows the unfolded FS under the triple- \mathbf{q} order below T_{DW} . In the present model, triple- \mathbf{q} order is expected to emerge because the momentum conservation $\mathbf{q}_1 + \mathbf{q}_2 + \mathbf{q}_3 = \mathbf{0}$ gives rise to the third-order Ginzburg-Landau (GL) free energy $F^{(3)} = b\phi_1\phi_2\phi_3$, where ϕ_n is real order parameter for $\mathbf{q} = \mathbf{q}_n$ bond-order ($n = 1-3$) [48]. Here, $\phi_n \hat{f}_{\mathbf{q}_n}(k)$ is the bond-order function, where $\hat{f}_{\mathbf{q}_n}(k)$ is the normalized dimensionless form factor given by the linearized DW equation. A more detailed explanation is given in the SM D.

We stress that the bond-order originates from the inter-sublattice VC in the kernel function I in Eq. (2). (Within the RPA, I ($= -U$) is an intra-sublattice function.) The dominant form factor at wavevector $\mathbf{q} = \mathbf{q}_1$, $f_{\mathbf{q}_1}^{lm}(\mathbf{k})$, is given by $(lm) = (AB)$ and (BA) . To understand its origin, we examine the kernel function at the lowest Matsubara frequency, multiplied with the b_{3g} -orbital weight (A , B , or C) on two conduction bands at four outer points, \tilde{I} . Results are shown in Figs. 3 (a) $\tilde{I}_{\mathbf{q}_1}^{AB,AB}(\mathbf{k}, \mathbf{k}_B)$ and (b) $\tilde{I}_{\mathbf{q}_1}^{BA,AB}(\mathbf{k}, \mathbf{k}_B)$, at $T = 0.02$ and $\alpha_S = 0.80$. They are obtained in the triangular lattice model in Fig. S1 that is equivalent to the kagome metal. We see the strong developments of (a) $g_{\text{back}} \equiv \tilde{I}_{\mathbf{q}_1}^{AB,AB}(\mathbf{k}_B, \mathbf{k}_B)$ and (b) $g_{\text{um}} \equiv \tilde{I}_{\mathbf{q}_1}^{BA,AB}(\mathbf{k}_A, \mathbf{k}_B)$, which correspond to the backward and umklapp scattering in Fig. 1 (f). (We note the relation $\mathbf{k}_A + \mathbf{q}_1 = \mathbf{k}_B$, and four outer momenta and sublattices of I are explained in the Method section.) Both scatterings contribute to the bond-order formation, as we clearly explain based on a simple two vHS model in SM B. Microscopic origin of

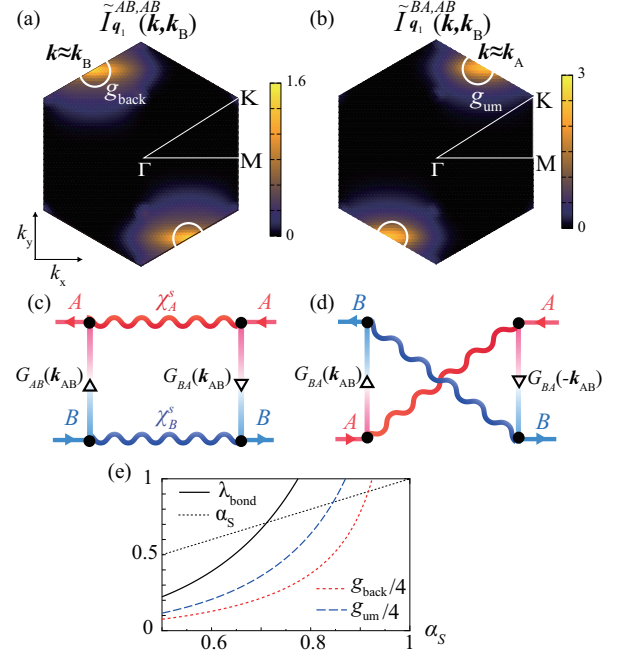


FIG. 3: **Origin of backward and umklapp scatterings that cause bond-order and SC state:** Kernel function in the DW equation with orbital weights at the lowest Matsubara frequency: (a) $\tilde{I}_{\mathbf{q}_1}^{AB,AB}(\mathbf{k}, \mathbf{k}_B)$ and (b) $\tilde{I}_{\mathbf{q}_1}^{BA,AB}(\mathbf{k}, \mathbf{k}_B)$ for $\alpha_S = 0.80$. In the kernel function, the outer momenta and sublattices are explained in the Method section. The former at $\mathbf{k} = \mathbf{k}_B$ and the latter at $\mathbf{k} = \mathbf{k}_A$ give g_{back} and g_{um} , respectively. Both scatterings contribute to the bond-order formation. (c) AL-VC with p-h pair and (d) that with p-p pair. The former (latter) gives large g_{back} (g_{um}). (e) λ_{bond} , g_{back} and g_{um} as functions of α_S at $T = 0.02$.

large g_{back} [g_{um}] is the AL-VC with p-h [particle-particle (p-p)] pair shown in Fig. 3 (c) [(d)], because of the relation $\chi_A^s, \chi_B^s \gg |\chi_{AA, BB}^s|$. They are included as AL1 and AL2 in the kernel function I ; see the Method section.

In Fig. 3 (e), we display the increment of λ_{bond} , g_{back} and g_{um} with α_S ($\propto U$) at $T = 0.02$. (The relation $\lambda_{\text{bond}} \propto g_{\text{back}} + g_{\text{um}}$ holds, as we explain in SM B.) When $\alpha_S = 0.75$, then $\lambda_{\text{bond}} \approx 0.88$, $g_{\text{um}} \approx 2$ and $g_{\text{back}} \approx 1$, respectively. Thus, both g_{um} and g_{back} are comparable or larger than U due to the quantum interference mechanism in Figs. 3 (c) and (d), in which the inter-orbital Green function $G_{AB}(k)$ is significant. As understood from Fig. 1 (b), $G_{AB}(k)$ is large at $\mathbf{k} \sim \mathbf{k}_{AB}$, while it vanishes at $\mathbf{k} = \mathbf{k}_A$ and \mathbf{k}_B . Therefore, the FS portion away from vHS points is indispensable in deriving the smectic order.

Unconventional superconductivity

Finally, we study the unconventional superconductivity mediated by bond-order fluctuations. Here, we solve

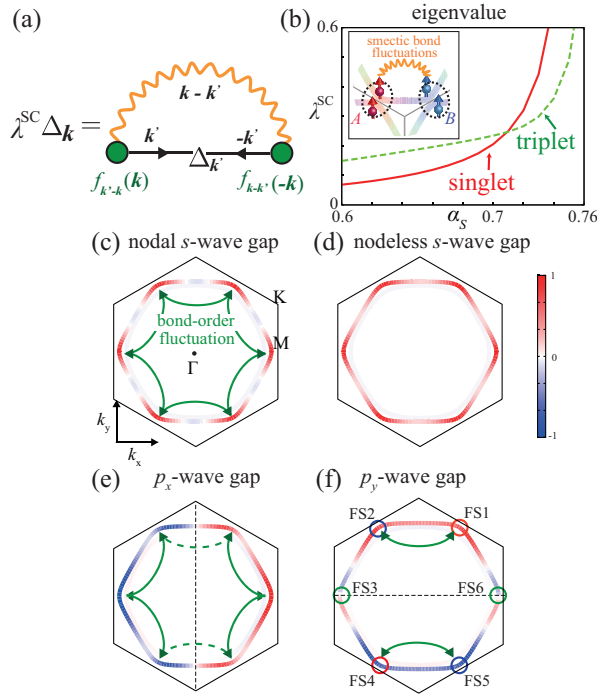


FIG. 4: Unconventional SC states due to bond-order fluctuation ‘beyond-Migdal’ pairing glue: (a) Pairing gap equation due to bond-order fluctuations. The form factor f gives the nonlocal (beyond-Migdal) electron-boson coupling function. (b) Obtained eigenvalues of gap equation for the singlet s -wave (A_{1g}) and the triplet p -wave (E_{1u}) states. Obtained gap functions: (c) nodal s -wave state ($\alpha_S = 0.75$), (d) nodeless s -wave state ($\alpha_S = 0.76$), and (e)(f) (p_x, p_y)-wave state ($\alpha_S = 0.70$). Green full (broken) arrow lines represent the smectic fluctuations between vHS points with the same (opposite) sign gap functions.

the following linearized SC gap equation on the FSs:

$$\lambda^{\text{SC}} \Delta_{\mathbf{k}}(\epsilon_n) = \frac{\pi T}{(2\pi)^2} \sum_{\epsilon_m} \oint_{\text{FSs}} \frac{d\mathbf{k}'}{v_{\mathbf{k}'}} \frac{\Delta_{\mathbf{k}'}(\epsilon_m)}{|\epsilon_m|} V_{s(t)}^{\text{SC}}(k, k'), \quad (4)$$

where $\Delta_{\mathbf{k}}(\epsilon_n)$ is the gap function on FSs, and $v_{\mathbf{k}}$ is the Fermi velocity. The eigenvalue λ^{SC} reaches unity at $T = T_c$. The diagrammatic expression of Eq. (4) is given in Fig. 4 (a). The form factor represents the ‘‘nonlocal’’ electron-boson coupling function that is a part of the beyond-Migdal effects. $V_{s(t)}^{\text{SC}}$ is the singlet/triplet pairing interaction in the band-basis, due to the triple- \mathbf{q} bond-order fluctuations (V_{bond}) and spin fluctuations ($\frac{3}{2}U^2\chi^s$) derived in SM E. Here, V_{bond} for $\mathbf{k}' - \mathbf{k} \approx \mathbf{q}_1$ is given as

$$\frac{1}{2} \frac{g_{\text{um}} \bar{f}_{\mathbf{q}_1}(\mathbf{k}) \bar{f}_{\mathbf{q}_1}(-\mathbf{k}')^*}{1 - \lambda_{\text{bond}}} \frac{1}{1 + \xi^2(\mathbf{q}_1 - (\mathbf{k}' - \mathbf{k}))^2}, \quad (5)$$

where $\bar{f}_{\mathbf{q}}(\mathbf{k})$ is the Hermite form factor in the band-basis, and $|\bar{f}_{\mathbf{q}_1}(\mathbf{k}_A)| = 1$. Both λ_{bond} and g_{um} are already obtained in Fig. 3 (e), and the numerator of Eq. (5) on outer FS is given in Fig. S6 in SM E.

Figure 4 (b) shows the obtained λ^{SC} at $T = 0.02$ and $\xi = 1.0$, where the s -wave singlet state appears when $\alpha_S \gtrsim 0.7$ and $\lambda_{\text{bond}} > \alpha_S$. Figures 4 (c) and (d) exhibit the obtained nodal s -wave gap function at $\alpha_S = 0.75$ ($\lambda_{\text{bond}} = 0.88$) and nodeless s -wave one at $\alpha_S = 0.76$ ($\lambda_{\text{bond}} = 0.92$), respectively. On the other hand, (p_x, p_y) -wave gap functions obtained at $\alpha_S = 0.70$ are shown in Figs. 4 (e) and (f). Note that obtained SC gap on inner FS made of b_{2g} -orbital is very small, while it can be large due to (for instance) finite inter-band electron-phonon interaction.

Here, we discuss the origin of the s/p -wave SC state. Triple- \mathbf{q} bond-order fluctuations work as attraction between FS i and FS $(i+1)$, where FS i ($i = 1 \sim 6$) is the FS portion around vHS points shown in Fig. 4 (f). Therefore, six pairs shown by green full arrows contribute to the s -wave state in Fig. 4 (c). In contrast, only two pairs contribute to the p_y -wave state in Fig. 4 (f). (In the p_x -wave state in Fig. 4 (e), four pairs (two pairs) give a positive (negative) contribution.) Therefore, the s -wave state is obtained for $\alpha_S \gtrsim 0.7$, where λ_{bond} exceeds α_S . In contrast, the p -wave state is obtained for $\alpha_S \lesssim 0.7$, because weak ferro-spin-fluctuations favor (destroy) the triplet (singlet) pairing. Thus, the present spin + bond-order fluctuation mechanism leads to rich s - and p -wave states. Possible SC states in the P - T phase diagram in CsV_3Sb_5 will be discussed in the Discussion section.

The nodal gap structure shown in Fig. 4 (c) is obtained in the case of $\alpha_S = 0.75$ ($U = 1.18$). We verified that the nodal s -wave gap structure emerges away from the vHS points so as to minimize the ‘‘depairing effect by moderately \mathbf{k} -dependent repulsion by weak spin fluctuations’’, which are shown in Fig. 1 (e). On the other hand, the nodeless s -wave state is realized when $\alpha_S = 0.76$, as shown in Fig. 4 (d). The reason is that the attraction due to bond-order susceptibility ($\propto 1/(1 - \lambda_{\text{bond}})$) is strongly enhanced with increasing for $\alpha_S \gtrsim 0.7$ as recognized in Fig. 3 (e), and therefore the reduction of depairing due to nodal structure becomes unnecessary.

To summarize, large attraction between different vHS points is induced by the bond-order fluctuations due to the paramagnon interference process. In contrast, the repulsion between different vHS points due to spin fluctuations is small, by reflecting the fact that the vHS points \mathbf{k}_A , \mathbf{k}_B , and \mathbf{k}_C are respectively composed of single orbital A, B, and C (= sublattice interference [34]). For this reason, moderate bond-order fluctuations ($\lambda_{\text{bond}} \gtrsim 0.9$) can induce nodeless s -wave SC gap state against spin fluctuations.

DISCUSSION

Importance of paramagnon interference

We have studied the exotic density-wave and beyond-Migdal unconventional superconductivity in kagome metal AV_3Sb_5 ($A=K, Rb, Cs$), by focusing on the paramagnon interference mechanism. This beyond-mean-field mechanism provides sizable “inter-sublattice” scattering, and therefore the smectic bond-order is realized in the presence of experimentally observed weak spin fluctuations. The bond-order fluctuations naturally mediate strong pairing glue that leads to the s -wave state, consistently with recent several experiments [20, 21, 29, 38]. Thus, the origins of the star of David order, the exotic superconductivity, and the strong interplay among them, are uniquely explained based on the paramagnon interference mechanism. This mechanism has been overlooked previously. This novel mechanism overcomes the difficulty of the sublattice interference [34], which leads to tiny inter-site interaction in weak-coupling theories, and gives rise to rich phase transitions in kagome metals. These key findings would promote future experiments on not only kagome metals, but also other frustrated metals.

A great merit of the present theory is that the bond-order is robustly obtained for a wide range of model parameters, as long as the bandstructure near the three vHS points is correctly reproduced. U is the only model parameter in the present theory. To clarify this merit, we make the comparison between the DW equation theory and mean-field theory. In the mean-field theory, the instability of the charge bond-order is always secondary even if large nearest-neighbor Coulomb interaction V is introduced. In contrast, in the DW equation theory, the charge bond-order solution is robustly obtained even when $V=0$. This is a great merit of the present DW equation analysis. This merit remains even if both charge- and spin-channel VCs are taken into account as explained in SM F.

We also discuss interesting similarities between kagome metal and other strongly correlated metals. The paramagnon interference mechanism has been successfully applied to explain the nematic and smectic orders in Fe-based and cuprate superconductors [4, 6]. However, they appear only in the vicinity of the magnetic criticality, except for FeSe systems [9, 10]. In contrast, the smectic bond-order in kagome metal appears irrespective of small spin fluctuations ($\alpha_S \sim 0.75$), because of the strong geometrical frustration inherent in kagome metals. The present study would be useful to understand the recently discovered “smectic order and adjacent high- T_c state” in FeSe/SrTiO₃ [56].

Impurity effect on superconductivity

The impurity effect is one of the most significant experiments to distinguish the symmetry of the SC gap function. However, experimental reports of the impurity effect on AV_3Sb_5 and its theoretical analysis have been limited so far. Here, we study the nonmagnetic impurity effect on both s -wave and p -wave SC states predicted in the present theory in Fig. 4. We treat the dilute V-site impurities based on the T-matrix approximation. The impurity potential on the A-site is $(\hat{I}_{\text{imp}}^A)_{ll'} = \delta_{l,l'}$, where $l, l' = A, A'$. In this case, the T-matrix on A-site is given by $\hat{T}^A = \hat{I}_{\text{imp}}^A (\hat{1} - \hat{g}^A \hat{I}_{\text{imp}}^A)^{-1}$, where \hat{g}^A is the 2×2 local Green function on A-site. In this case, the normal self-energy is given by $\hat{\Sigma}^n = n_{\text{imp}} (\hat{T}^A + \hat{T}^B + \hat{T}^C)$, where n_{imp} is the impurity concentration. The anomalous self-energy is also given by the T-matrix. Here, we consider the unitary limit case ($I_{\text{imp}} = \infty$). More detailed explanation is written in Ref. [57].

Figure 5 (a) shows the changes of the nodal s -wave SC gap function due to the impurity effect at $\alpha_S = 0.75$. The gap function at $n_{\text{imp}} = 0$ is the same as Fig. 4 (c). The accidental nodes at $n_{\text{imp}} = 0$ are lifted up due to the impurities, and the nodeless s -wave gap emerges at just $n_{\text{imp}} = 0.02$. The ratio of the minimum gap over the maximum one quickly increases with n_{imp} as plotted in Fig. 5 (b). Figure 5 (c) shows the eigenvalues of the s -wave (λ_s^{SC}) and p -wave SC states (λ_p^{SC}). Note that $\lambda_{s(p)}^{\text{SC}}$ is proportional to $s(p)$ -wave T_c . (Here, the pairing interaction for the p -wave SC is magnified by 2.7 to make both λ_s^{SC} and λ_p^{SC} comparable.) λ_p^{SC} drastically decreases with n_{imp} by following the Abrikosov-Gorkov theory. In contrast, the reduction in λ_s^{SC} is much slower, and its suppression saturates when the gap becomes nearly isotropic for $n_{\text{imp}} \gtrsim 0.05$.

The obtained impurity-induced drastic change in the gap anisotropy is a hallmark of the s -wave SC mediated by the bond-order fluctuations. Thus, measurements of the impurity effects will be very promising toward the whole understanding of the SC phase. Note that when the p -wave SC state appears at $n_{\text{imp}} = 0$, the transition from p -wave to s -wave state is caused by introducing dilute impurities.

P-T phase diagram

We discuss the P - T phase diagram of CsV_3Sb_5 , in which the SC phase shows the highest $T_c \sim 8$ K at the critical pressure $P_{c2} \sim 2$ GPa ($T_{\text{DW}} = 0$) [15]. Inside the bond-order phase, the second highest SC dome with $T_c \sim 6$ K emerges at $P_{c1} \sim 0.7$ GPa. Between P_{c1} and P_{c2} , both T_c and the SC volume fraction are reduced, while the residual resistivity increases. As discussed in Ref. [15], these states remind us of the inhomogeneous

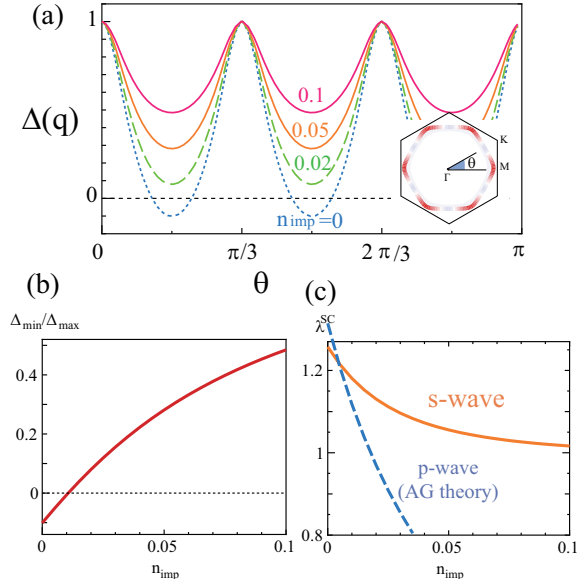


FIG. 5: **Impurity effect on superconductivity:** (a) Obtained nodal *s*-wave gap function at $n_{\text{imp}} = 0 - 0.1$. (b) n_{imp} -dependence of $\Delta_{\text{min}}/\Delta_{\text{max}}$ in the *s*-wave state. (c) n_{imp} -dependence of the eigenvalue of *s*-wave and *p*-wave SC states. *s*-wave superconductivity is robust against the impurity effect, while the *p*-wave one is quite weak. (Here, *p*-wave pairing interaction is magnified by 2.7.)

“nearly-commensurate CDW (NCCDW)” in 1T-TaS₂, which is realized when the correlation-driven incommensurate DW order at the FS nesting vector [48] is partially locked to the lattice via the electron-phonon interaction. When such an inhomogeneous DW state appears, T_c of strongly anisotropic SC gap state should be suppressed, so the double-dome SC structure is realized.

To support this NCCDW scenario for $P > P_{c1}$ [15], we construct realistic tight-binding models at 0 – 3GPa based on the first-principles study, which are constructed by using Wien2k and Wannier90 software [58]. Figure 6 (a) shows the FSs at $P = 0$: The b_{3g} -orbital FS is essentially similar to that in Fig. 1 (d). Interestingly, the b_{3g} -FS at 3GPa becomes smaller due to the pressure-induced self-doping on b_{3g} -FS ($\sim 1.5\%$), deviating from the vHS points as illustrated in Fig. 6 (b). (The change in k_F on k_x -axis is $\Delta k_F = -0.02\pi$.) The obtained change is reliable because it is derived from the first-principles “pressure Hamiltonian $\Delta H_0^{\text{DFT}}(P)$ ” given in the SM G. The present discovered P -dependence in the FS and its nesting vector would cause the C-IC bond-order transition.

Based on the derived realistic models, we perform the DW equation analysis. Figure 6 (c) shows the obtained \mathbf{q} -dependent eigenvalue, $\lambda_{\mathbf{q}}$, at 0 – 3GPa with $T = 0.04$ [eV] and $U = 2.7$ [eV]. At $P = 0$, we obtain the commensurate bond-order (CBO) solution at $\mathbf{q} = \mathbf{q}_1$, so the robustness of the bond-order solution in Fig. 2 is confirmed. On

the other hand, $\lambda_{\mathbf{q}_1}$ is quickly suppressed under pressure (over 30% at 3GPa). Since $T_{\text{DW}} \propto \lambda_{\mathbf{q}_1}$ qualitatively, this result is consistent with the strong suppression of the bond-order under pressure in kagome metals. In the interference mechanism, small reduction in α_S induced by the pressure (just ~ 0.03 at 3GPa) causes sizable suppression of $\lambda_{\mathbf{q}_1}$, as we can see in Fig. 2 (b). Interestingly, the CBO at $P = 0$ turns to be incommensurate one at $\mathbf{q} = \mathbf{q}_1 + (0, \delta)$ when $P \gtrsim 1$ GPa, by reflecting the change in the nesting condition. The P -dependence of the bond-order eigenvalues is summarized in Fig. 6 (d).

In SM B, we examine the filling-dependence of the bond-order solution in the present six orbital kagome lattice model. As shown in Fig. S3 (b), the C-IC bond-order transition occurs at $n = n_0 \equiv 3.82$. For $n > n_0$, the incommensurate bond-order (ICBO) is realized due to the change in the Fermi momentum Δk_F . Thus, the C-IC transition can also be understood in the present simple six orbital model. The present theory supports the NC-CDW scenario discussed in Ref. [15].

Next, we propose a possible scenario for the double-dome SC phase on AV₃Sb₅. The phase diagram based on the present scenario is schematically represented in Fig. 6 (e). The present bond-order fluctuation-mediated *s*-wave state should exhibit the highest- T_c around the critical pressure $P = P_{c2}$. Thus, the T_c monotonically decreases as $|P - P_{c2}|$ increases. In addition, the NCCDW-like inhomogeneous states triggered by the ICBO formation lead to the dip structure in T_c for $P \gtrsim P_{c1}$. Therefore, the double-dome SC phase is naturally explained in terms of the C-IC bond-order transition.

In another SC dome for $P < P_{c1}$, both *p*- and *s*-wave SC can emerge because bond-order and spin fluctuations would be comparable. If the *p*-wave SC state is realized at $n_{\text{imp}} = 0$, the *p*-wave to *s*-wave SC transition will occur at $n_{\text{imp}} \sim 0.01$ as understood in Fig. 5 (c).

Future problems

In kagome metals, the bond-order state is the platform of various exotic phenomena. In this respect, the mechanism of the bond-order state should be clarified in kagome metal. The discovered quantum interference process in the present study triggers the bond-order formation, and this process would be important even below T_{DW} . Thus, the present study paved the way for understanding the whole phase diagram.

A central open problem in the bond-order state is the time-reversal-symmetry-breaking (TRSB) state. In AV₃Sb₅, the TRSB state has been reported by STM, Kerr effect and μ SR measurements in Refs. [31, 59, 60]. The $T_{\text{TRSB}} \sim 70$ K is suggested by μ SR study, while $T_{\text{TRSB}} = T_{\text{DW}} = 94$ K is reported by Kerr effect [31, 60]. The leading candidate for the TRSB is the charge LC order that accompanies the local magnetic field, as studied

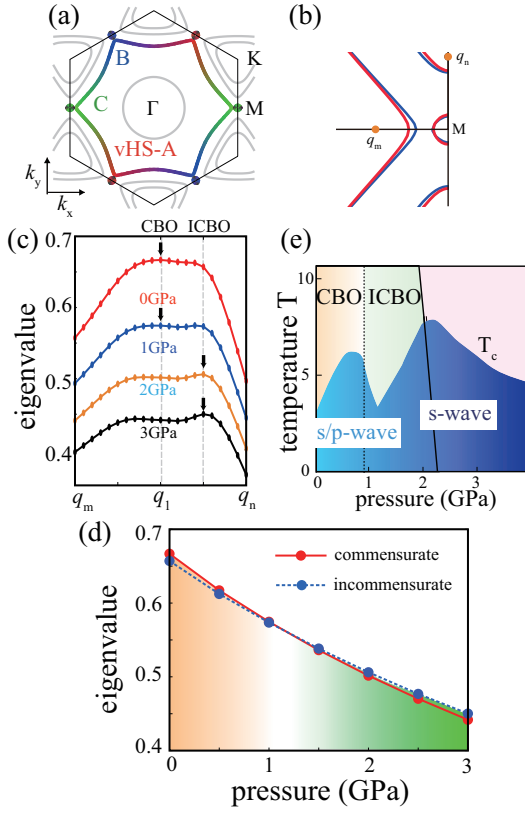


FIG. 6: Pressure-induced C-IC bond-order transition.
 (a) FSs in the realistic 30 orbital model at $P = 0$. The b_{3g} -orbital weight on A (red), B (blue), and C (green) sublattices are shown. (b) FSs around vHS points at $P = 0$ and 3GPa. (c) Obtained \mathbf{q} -dependence of the eigenvalue for bond-order at $0 \sim 3$ GPa. Here, CBO (ICBO) means the commensurate (incommensurate) bond-order. (d) Pressure dependence of the eigenvalue of the bond-order. The C-IC transition emerges around $P \sim 1$ GPa. (e) Schematic P - T phase diagram derived from the present theory.

in cuprates for a long time [61, 62].

However, the microscopic mechanism of the LC order has been unsolved. For example, the LC phase does not appear in the U - V phase diagram in the mean-field approximation in Fig. S7. Thus, beyond-mean-field analysis is required to solve this open issue. An important clue is given by the spin-fluctuation-driven LC mechanism in frustrated metals in Refs. [63, 64]. This beyond-mean-field LC mechanism is general because the LC is caused by various spin/charge-channel fluctuations. Thus, new spin/charge-channel fluctuations due to the FS reconstruction below T_{DW} may induce the LC order in the bond-order state. Therefore, the present bond-order theory provides a significant starting point to understand the phase diagram of AV_3Sb_5 .

The coexistence of the LC and the bond-order is predicted based on GL theory in Ref. [28]. Interestingly, the relation $T_{\text{TRSB}} \sim T_{\text{DW}}$ is realized when the third-order term in the GL free energy, inherent in kagome metals,

is sizable. In future, it is useful to solve the “full DW equation without linearization”, in which effect of the third-order GL term is included.

Another important issue is the anomalous transport phenomena below T_{DW} . For instance, giant anomalous Hall effect [65, 66] is observed in several kagome metals. In addition, sizable thermoelectric power and Nernst effect are reported [67]. These transport coefficients can be calculated based on the realistic tight-binding models in Fig. 6, under the presence of the bond-order and the LC order. The VCs for the current due to spin/charge fluctuations would play significant roles [68]. It is an useful future problem to study the effect of the three-dimensionality on the electronic states in kagome metals.

MATERIALS AND METHODS

Derivation of density-wave equation

Here, we derive the kernel function in the DW equation, $I_q^{ll',mm'}(k, k')$, studied in the main text. It is given as $\delta^2 \Phi_{\text{LW}} / \delta G_{ll'}(k) \delta G_{mm'}(p)$ at $\mathbf{q} = \mathbf{0}$ in the conserving approximation scheme [44, 55], where Φ_{LW} is the Luttinger-Ward function. Here, we apply the one-loop approximation for Φ_{LW} [6, 44]. Then, $I_q^{L,M}$ in this kagome model is given as

$$\begin{aligned}
 I_q^{ll',mm'}(k, k') = & \sum_{b=s,c} \frac{a^b}{2} \left[-V_{lm,l'm'}^b(k - k') \right. \\
 & + \frac{T}{N} \sum_p \sum_{l_1 l_2, m_1 m_2} V_{ll_1,mm_1}^b(p + \mathbf{q}) V_{m'm_2,l'l_2}^b(p) \\
 & \quad \times G_{l_1 l_2}(k - p) G_{m_2 m_1}(k' - p) \\
 & + \frac{T}{N} \sum_p \sum_{l_1 l_2, m_1 m_2} V_{ll_1,m_2 m'}^b(p + \mathbf{q}) V_{m_1 m,l'l_2}^b(p) \\
 & \quad \left. \times G_{l_1 l_2}(k - p) G_{m_2 m_1}(k' + p + \mathbf{q}) \right], \quad (6)
 \end{aligned}$$

where $a^{s(c)} = 3(1)$ and $p = (\mathbf{p}, \omega_l)$. \hat{V}^b is the b -channel interaction given by $\hat{V}^b = \hat{U}^b + \hat{U}^b \hat{\chi}^b \hat{U}^b$. \hat{U}^b is the matrix expression of the bare multiorbital Coulomb interaction for channel b .

Under the uniform ($\mathbf{q} = \mathbf{0}$) DW state, the one-loop Φ_{LW} is given as $\Phi_{\text{LW}} = T \sum_p \left[\frac{3}{2} \text{Tr} \ln(\hat{1} - \hat{U}^s \hat{\chi}^0(p)) + \frac{1}{2} \text{Tr} \ln(\hat{1} - \hat{U}^c \hat{\chi}^0(p)) \right]$ with the correction terms up to $O(U^2)$. When the wavevector \mathbf{q} of the DW state is nonzero, $\hat{\chi}^0(p)$ is replaced with $\hat{\chi}^0(p; q)$.

The first term of Eq. (6) corresponds to the single-magnon exchange Maki-Thompson term, and the second and third terms give two double-magnon interference AL terms. They are expressed in Fig. 7 (a).

The DW instability driven by nonlocal beyond-mean-field correlation $\hat{I}_q(k, k')$ is obtained by solving the DW

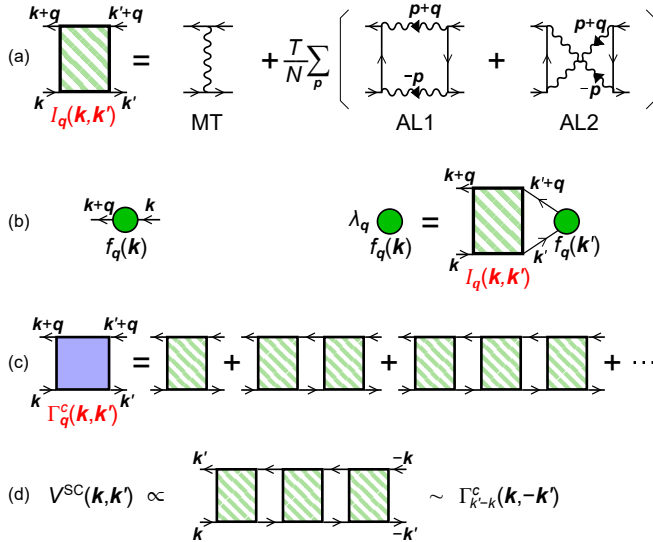


FIG. 7: **Derivations of DW equation and beyond-Migdal pairing interaction:** (a) Charge-channel kernel function $I_q^{ll',mm'}(k,k')$ (b) Linearized DW equation. (c) Charge-channel full four-point vertex $\Gamma_q^c(k,k')$ obtained by solving the DW equation. (d) Pairing interaction due to Γ_q^c : $V^{SC}(k,k') \propto \Gamma_{k'-k}^c(k,-k')$.

equation introduced in Refs. [10, 44, 47]:

$$\begin{aligned} \lambda_q f_q^{ll'}(k) &= \frac{T}{N} \sum_{k',m,m'} K_q^{ll',mm'}(k,k') f_q^{mm'}(k') \quad (7) \\ K_q^{ll',mm'}(k,k') &= - \sum_{m'',m'''} I_q^{ll',m'',m'''}(k,k') \\ &\quad \times G_{m''m}(k' + \mathbf{q}) G_{m'm'''}(k'), \quad (8) \end{aligned}$$

which is depicted in Fig. 7 (b). Here, λ_q is the eigenvalue that reaches unity at the transition temperature. \hat{f}_q is the form factor of the DW order, which corresponds to the “symmetry-breaking in the self-energy”. By solving Eq. (7), we can obtain the optimized momentum and orbital dependences of \hat{f} . This mechanism has been successfully applied to explain the electronic nematic orders in Fe-based [6, 9, 10] and cuprate superconductors [4], and multipole orders in f -electron systems [49].

An arbitrary phase factor $e^{i\alpha}$ can be multiplied to the solution of the linearized DW equation $\hat{f}_q(k)$. However, the phase factor should be determined uniquely so that $\hat{f}_q(k) = (\hat{f}_q(k, \pi T) + \hat{f}_q(k, -\pi T))/2$ satisfies the Hermite condition $\hat{f}_q^{lm}(k) = [f_{-q}^{ml}(k + \mathbf{q})]^*$.

Finally, we discuss the effective interaction driven by the bond-order fluctuations. By solving the DW equation (7), we obtain the full four-point vertex function $\Gamma_q^c(k,k')$ that is composed of I_q^c and $G(k + \mathbf{q})G(k)$ shown in Fig. 7 (c), which increases in proportion to $(1 - \lambda_q)^{-1}$. Thus, we obtain the relation $\Gamma_q^c(k,k') \approx f_q(k)\{f_q(k')\}^* \bar{I}_q^c(1 - \lambda_q)^{-1}$, which is well satisfied when λ_q is close to unity.

As we will discuss in SM E, the pairing interac-

tion due to the bond-order fluctuations is given by the full four-point vertex: $V^{SC}(k,k') \sim \Gamma_{k'-k}^c(k, -k') \sim f_{k'-k}(k)\{f_{k'-k}(-k')\}^*(1 - \lambda_q)^{-1}$, which is depicted in Fig. 7 (d).

It is noteworthy that both the DW equation and the fRG method explain the nematic and smectic bond-order in single-orbital square lattice Hubbard models [46, 47] and anisotropic triangular lattice ones [4]. This fact means that higher-order diagrams other than MT or AL terms, that are included in the fRG method, are not essential in explaining the bond-order. Note that the contributions away from the conduction bands are included into N -patch fRG by applying the RG+cRPA method [4, 46, 46].

- [1] E. Fradkin and S. A. Kivelson, Ineluctable complexity, *Nat. Phys.* **8**, 864 (2012).
- [2] J. C. S. Davis and D.-H. Lee, Concepts relating magnetic interactions, intertwined electronic orders, and strongly correlated superconductivity, *Proc. Natl. Acad. Sci. U.S.A.* **110**, 17623 (2013).
- [3] T. Shibauchi, T. Hanaguri, and Y. Matsuda, Exotic Superconducting States in FeSe-based Materials, *J. Phys. Soc. Jpn.* **89**, 102002 (2020).
- [4] R. Tazai, Y. Yamakawa, M. Tsuchiizu, and H. Kontani, d - and p -wave Quantum Liquid Crystal Orders in Cuprate Superconductors, κ -(BEDT-TTF)₂X, and Coupled Chain Hubbard Models: Functional-renormalization-group Analysis, *J. Phys. Soc. Jpn.* **90**, 111012 (2021).
- [5] H. Kontani, T. Saito, and S. Onari, Origin of orthorhombic transition, magnetic transition, and shear-modulus softening in iron pnictide superconductors: Analysis based on the orbital fluctuations theory, *Phys. Rev. B* **84**, 024528 (2011).
- [6] S. Onari and H. Kontani, Self-consistent Vertex Correction Analysis for Iron-based Superconductors: Mechanism of Coulomb Interaction-Driven Orbital Fluctuations, *Phys. Rev. Lett.* **109**, 137001 (2012).
- [7] M. Tsuchiizu, Y. Ohno, S. Onari, and H. Kontani, Orbital Nematic Instability in the Two-Orbital Hubbard Model: Renormalization-Group + Constrained RPA Analysis, *Phys. Rev. Lett.* **111**, 057003 (2013).
- [8] Y. Yamakawa and H. Kontani, Spin-Fluctuation-Driven Nematic Charge-Density Wave in Cuprate Superconductors: Impact of Aslamazov-Larkin Vertex Corrections, *Phys. Rev. Lett.* **114**, 257001 (2015).
- [9] Y. Yamakawa, S. Onari, and H. Kontani, Nematicity and Magnetism in FeSe and Other Families of Fe-Based Superconductors, *Phys. Rev. X* **6**, 021032 (2016).
- [10] S. Onari, Y. Yamakawa, and H. Kontani, Sign-Reversing Orbital Polarization in the Nematic Phase of FeSe due to the C_2 Symmetry Breaking in the Self-Energy, *Phys. Rev. Lett.* **116**, 227001 (2016).
- [11] A. V. Chubukov, M. Khodas, and R. M. Fernandes, Magnetism, Superconductivity, and Spontaneous Orbital Order in Iron-Based Superconductors: Which Comes First and Why?, *Phys. Rev. X* **6**, 041045 (2016).

[12] R. M. Fernandes, P. P. Orth, J. Schmalian, Intertwined Vestigial Order in Quantum Materials: Nematicity and Beyond. *Annual Review of Condensed Matter Physics* **10**, 133-154 (2019).

[13] B. R. Ortiz, L. C. Gomes, J. R. Morey, M. Winiarski, M. Bordelon, J. S. Mangum, I. W. H. Oswald, J. A. Rodriguez-Rivera, J. R. Neilson, S. D. Wilson, E. Ertekin, T. M. McQueen, and E. S. Toberer, New kagome prototype materials: discovery of KV_3Sb_5 , RbV_3Sb_5 , and CsV_3Sb_5 , *Phys. Rev. Materials* **3**, 094407 (2019).

[14] B. R. Ortiz, S. M. L. Teicher, Y. Hu, J. L. Zuo, P. M. Sarte, E. C. Schueller, A. M. M. Abeykoon, M. J. Krogstad, S. Rosenkranz, R. Osborn, R. Seshadri, L. Balents, J. He, and S. D. Wilson, CsV_3Sb_5 : A \mathbb{Z}_2 Topological Kagome Metal with a Superconducting Ground State, *Phys. Rev. Lett.* **125**, 247002 (2020).

[15] F. H. Yu, D. H. Ma, W. Z. Zhuo, S. Q. Liu, X. K. Wen, B. Lei, J. J. Ying, and X. H. Chen, Unusual competition of superconductivity and charge-density-wave state in a compressed topological kagome metal, *Nat. Commun.* **12**, 3645 (2021).

[16] K. Y. Chen, N. N. Wang, Q. W. Yin, Y. H. Gu, K. Jiang, Z. J. Tu, C. S. Gong, Y. Uwatoko, J. P. Sun, H. C. Lei, J. P. Hu, and J.-G. Cheng, Double Superconducting Dome and Triple Enhancement of T_c in the Kagome Superconductor CsV_3Sb_5 under High Pressure, *Phys. Rev. Lett.* **126**, 247001 (2021).

[17] B. R. Ortiz, P. M. Sarte, E. M. Kenney, M. J. Graf, S. M. L. Teicher, R. Seshadri, and S. D. Wilson, Superconductivity in the \mathbb{Z}_2 kagome metal KV_3Sb_5 , *Phys. Rev. Materials* **5**, 034801 (2021).

[18] Q. Yin, Z. Tu, C. Gong, Y. Fu, S. Yan, and H. Lei, Superconductivity and Normal-State Properties of Kagome Metal RbV_3Sb_5 Single Crystals, *Chin. Phys. Lett.* **38**, 037403 (2021).

[19] C. C. Zhao, L. S. Wang, W. Xia, Q. W. Yin, J. M. Ni, Y. Y. Huang, C. P. Tu, Z. C. Tao, Z. J. Tu, C. S. Gong, H. C. Lei, Y. F. Guo, X. F. Yang, and S. Y. Li, Nodal superconductivity and superconducting domes in the topological Kagome metal CsV_3Sb_5 , arXiv:2102.08356 (available at <https://arxiv.org/abs/2102.08356>).

[20] W. Duan, Z. Nie, S. Luo, F. Yu, B. R. Ortiz, L. Yin, H. Su, F. Du, A. Wang, Y. Chen, X. Lu, J. Ying, S. D. Wilson, X. Chen, Y. Song, and H. Yuan, Nodeless superconductivity in the kagome metal CsV_3Sb_5 , *Sci. China Phys. Mech. Astron.* **64**, 107462 (2021).

[21] R. Gupta, D. Das, C. H. M. I. au2, Z. Guguchia, T. Shiroka, C. Baines, M. Bartkowiak, H. Luetkens, R. Khasanov, Q. Yin, Z. Tu, C. Gong, and H. Lei, Microscopic evidence for anisotropic multi-gap superconductivity in the CsV_3Sb_5 kagome superconductor, arXiv:2108.01574 (available at <https://arxiv.org/abs/2108.01574>).

[22] R. Lou, A. Fedorov, Q. Yin, A. Kuibarov, Z. Tu, C. Gong, E. F. Schwier, B. Büchner, H. Lei, and S. Borisenko, Charge-Density-Wave-Induced Peak-Dip-Hump Structure and Flat Band in the Kagome Superconductor CsV_3Sb_5 , arXiv:2106.06497 (available at <https://arxiv.org/abs/2106.06497>).

[23] T. Park, M. Ye, and L. Balents, Electronic instabilities of kagome metals: Saddle points and Landau theory, *Phys. Rev. B* **104**, 035142 (2021).

[24] H. Tan, Y. Liu, Z. Wang, and B. Yan, Charge Density Waves and Electronic Properties of Superconducting Kagome Metals, *Phys. Rev. Lett.* **127**, 046401 (2021).

[25] X. Wu, T. Schwemmer, T. Müller, A. Consiglio, G. Sangiovanni, D. Di Sante, Y. Iqbal, W. Hanke, A. P. Schnyder, M. M. Denner, M. H. Fischer, T. Neupert, and R. Thomale, Nature of Unconventional Pairing in the Kagome Superconductors AV_3Sb_5 ($A = \text{K}, \text{Rb}, \text{Cs}$), *Phys. Rev. Lett.* **127**, 177001 (2021).

[26] M. M. Denner, R. Thomale, and T. Neupert, Analysis of Charge Order in the Kagome Metal AV_3Sb_5 ($A = \text{K}, \text{Rb}, \text{Cs}$), *Phys. Rev. Lett.* **127**, 217601 (2021).

[27] C. Setty, H. Hu, L. Chen, and Q. Si, Electron correlations and T -breaking density wave order in a \mathbb{Z}_2 kagome metal, arXiv:2105.15204 (available at <https://arxiv.org/abs/2105.15204>).

[28] Y.-P. Lin and R. M. Nandkishore, Complex charge density waves at Van Hove singularity on hexagonal lattices: Haldane-model phase diagram and potential realization in the kagome metals AV_3Sb_5 ($A=\text{K}, \text{Rb}, \text{Cs}$), *Phys. Rev. B* **104**, 045122 (2021).

[29] C. Mu, Q. Yin, Z. Tu, C. Gong, H. Lei, Z. Li, and J. Luo, S-Wave Superconductivity in Kagome Metal CsV_3Sb_5 Revealed by $^{121/123}\text{Sb}$ NQR and ^{51}V NMR Measurements, *Chin. Phys. Lett.* **38**, 077402 (2021).

[30] D. W. Song, L. X. Zheng, F. H. Yu, J. Li, L. P. Nie, M. Shan, D. Zhao, S. J. Li, B. L. Kang, Z. M. Wu, Y. B. Zhou, K. L. Sun, K. Liu, X. G. Luo, Z. Y. Wang, J. J. Ying, X. G. Wan, T. Wu, and X. H. Chen, Orbital ordering and fluctuations in a kagome superconductor CsV_3Sb_5 , arXiv:2104.09173 (available at <https://arxiv.org/abs/2104.09173>).

[31] Y.-X. Jiang, J.-X. Yin, M. M. Denner, N. Shumiya, B. R. Ortiz, G. Xu, Z. Guguchia, J. He, M. S. Hossain, X. Liu, J. Ruff, L. Kautzsch, S. S. Zhang, G. Chang, I. Belopolski, Q. Zhang, T. A. Cochran, D. Multer, M. Litskevich, Z.-J. Cheng, X. P. Yang, Z. Wang, R. Thomale, T. Neupert, S. D. Wilson, and M. Z. Hasan, Unconventional chiral charge order in kagome superconductor KV_3Sb_5 , *Nat. Mater.* **20**, 1353 (2021).

[32] H. Li, H. Zhao, B. R. Ortiz, T. Park, M. Ye, L. Balents, Z. Wang, S. D. Wilson, and I. Zeljkovic, Rotation symmetry breaking in the normal state of a kagome superconductor KV_3Sb_5 , arXiv:2104.08209 (available at <https://arxiv.org/abs/2104.08209>).

[33] H. Li, T. T. Zhang, T. Yilmaz, Y. Y. Pai, C. E. Marinney, A. Said, Q. W. Yin, C. S. Gong, Z. J. Tu, E. Vescovo, C. S. Nelson, R. G. Moore, S. Murakami, H. C. Lei, H. N. Lee, B. J. Lawrie, and H. Miao, Observation of Unconventional Charge Density Wave without Acoustic Phonon Anomaly in Kagome Superconductors AV_3Sb_5 ($A = \text{Rb}, \text{Cs}$), *Phys. Rev. X* **11**, 031050 (2021).

[34] M. L. Kiesel, C. Platt, and R. Thomale, Unconventional Fermi Surface Instabilities in the Kagome Hubbard Model, *Phys. Rev. Lett.* **110**, 126405 (2013).

[35] W.-S. Wang, Z.-Z. Li, Y.-Y. Xiang, and Q.-H. Wang, Competing electronic orders on kagome lattices at van Hove filling, *Phys. Rev. B* **87**, 115135 (2013).

[36] J. Wen, A. Rüegg, C.-C. J. Wang, and G. A. Fiete, Interaction-driven topological insulators on the kagome and the decorated honeycomb lattices, *Phys. Rev. B* **82**, 075125 (2010).

[37] E. M. Kenney, B. R. Ortiz, C. Wang, S. D. Wilson, and M. J. Graf, Absence of local moments in the kagome metal KV_3Sb_5 as determined by muon spin spectroscopy,

J. Phys.: Condens. Matter **33**, 235801 (2021).

[38] H.-S. Xu, Y.-J. Yan, R. Yin, W. Xia, S. Fang, Z. Chen, Y. Li, W. Yang, Y. Guo, and D.-L. Feng, Multiband Superconductivity with Sign-Preserving Order Parameter in Kagome Superconductor CsV_3Sb_5 , *Phys. Rev. Lett.* **127**, 187004 (2021).

[39] Y. Wang, S. Yang, P. K. Sivakumar, B. R. Ortiz, S. M. L. Teicher, H. Wu, A. K. Srivastava, C. Garg, D. Liu, S. S. P. Parkin, E. S. Toberer, T. McQueen, S. D. Wilson, and M. N. Ali, Proximity-induced spin-triplet superconductivity and edge supercurrent in the topological Kagome metal, $\text{K}_{1-x}\text{V}_3\text{Sb}_5$, arXiv:2012.05898 (available at <https://arxiv.org/abs/2012.05898>).

[40] S. Ni, S. Ma, Y. Zhang, J. Yuan, H. Yang, Z. Lu, N. Wang, J. Sun, Z. Zhao, D. Li, S. Liu, H. Zhang, H. Chen, K. Jin, J. Cheng, L. Yu, F. Zhou, X. Dong, J. Hu, H.-J. Gao, and Z. Zhao, Anisotropic Superconducting Properties of Kagome Metal CsV_3Sb_5 , *Chin. Phys. Lett.* **38**, 057403 (2021).

[41] Y. Xiang, Q. Li, Y. Li, W. Xie, H. Yang, Z. Wang, Y. Yao, and H.-H. Wen, Twofold symmetry of c-axis resistivity in topological kagome superconductor CsV_3Sb_5 with in-plane rotating magnetic field, *Nat. Commun.* **12**, 6727 (2021).

[42] Z. Liang, X. Hou, F. Zhang, W. Ma, P. Wu, Z. Zhang, F. Yu, J.-J. Ying, K. Jiang, L. Shan, Z. Wang, and X.-H. Chen, Three-Dimensional Charge Density Wave and Surface-Dependent Vortex-Core States in a Kagome Superconductor CsV_3Sb_5 , *Phys. Rev. X* **11**, 031026 (2021).

[43] R. Tazai and H. Kontani, Fully gapped *s*-wave superconductivity enhanced by magnetic criticality in heavy-fermion systems, *Phys. Rev. B* **98**, 205107 (2018).

[44] S. Onari and H. Kontani, Hidden antiferromagnetic order in Fe-based superconductor BaFe_2As_2 and NaFeAs above T_c , *Phys. Rev. Research* **2**, 042005(R) (2020).

[45] A. V. Chubukov and P. Wölfle, Quasiparticle interaction function in a two-dimensional Fermi liquid near an antiferromagnetic critical point, *Phys. Rev. B* **89**, 045108 (2014).

[46] M. Tsuchiizu, K. Kawaguchi, Y. Yamakawa, and H. Kontani, Multistage electronic nematic transitions in cuprate superconductors: A functional-renormalization-group analysis, *Phys. Rev. B* **97**, 165131 (2018).

[47] K. Kawaguchi, Y. Yamakawa, M. Tsuchiizu, and H. Kontani, Competing Unconventional Charge-Density-Wave States in Cuprate Superconductors: Spin-Fluctuation-Driven Mechanism, *J. Phys. Soc. Jpn.* **86**, 063707 (2017).

[48] T. Hirata, Y. Yamakawa, S. Onari, and H. Kontani, Unconventional orbital charge density wave mechanism in the transition metal dichalcogenide $1T\text{-TaS}_2$, *Phys. Rev. Research* **3**, L032053 (2021).

[49] R. Tazai and H. Kontani, Multipole fluctuation theory for heavy fermion systems: Application to multipole orders in CeB_6 , *Phys. Rev. B* **100**, 241103(R) (2019).

[50] K. Nakayama, Y. Li, T. Kato, M. Liu, Z. Wang, T. Takahashi, Y. Yao, and T. Sato, Multiple energy scales and anisotropic energy gap in the charge-density-wave phase of the kagome superconductor CsV_3Sb_5 , *Phys. Rev. B* **104**, L161112 (2021).

[51] Z. Liu, N. Zhao, Q. Yin, C. Gong, Z. Tu, M. Li, W. Song, Z. Liu, D. Shen, Y. Huang, K. Liu, H. Lei, and S. Wang, Charge-Density-Wave-Induced Bands Renormalization and Energy Gaps in a Kagome Superconductor RbV_3Sb_5 , *Phys. Rev. X* **11**, 041010 (2021).

[52] Z. Wang, S. Ma, Y. Zhang, H. Yang, Z. Zhao, Y. Ou, Y. Zhu, S. Ni, Z. Lu, H. Chen, K. Jiang, L. Yu, Y. Zhang, X. Dong, J. Hu, H.-J. Gao, and Z. Zhao, Distinctive momentum dependent charge-density-wave gap observed in CsV_3Sb_5 superconductor with topological Kagome lattice, arXiv:2104.05556 (available at <https://arxiv.org/abs/2104.05556>).

[53] Y. Hu, X. Wu, B. R. Ortiz, S. Ju, X. Han, J. Z. Ma, N. C. Plumb, M. Radovic, R. Thomale, S. D. Wilson, A. P. Schnyder, and M. Shi, Rich Nature of Van Hove Singularities in Kagome Superconductor CsV_3Sb_5 , arXiv:2106.05922 (available at <https://arxiv.org/abs/2106.05922>).

[54] Y. Luo, S. Peng, S. M. L. Teicher, L. Huai, Y. Hu, B. R. Ortiz, Z. Wei, J. Shen, Z. Ou, B. Wang, Y. Miao, M. Guo, M. Shi, S. D. Wilson, and J.-F. He, Distinct band reconstructions in kagome superconductor CsV_3Sb_5 , arXiv:2106.01248 (available at <https://arxiv.org/abs/2106.01248>).

[55] G. Baym, Self-Consistent Approximations in Many-Body Systems, *Phys. Rev.* **127**, 1391 (1962).

[56] Y. Yuan, X. Fan, X. Wang, K. He, Y. Zhang, Q.-K. Xue, and W. Li, Incommensurate smectic phase in close proximity to the high- T_c superconductor $\text{FeSe}/\text{SrTiO}_3$, *Nat. Commun.* **12**, 2196 (2021).

[57] H. Kontani and S. Onari, Orbital-Fluctuation-Mediated Superconductivity in Iron Pnictides: Analysis of the Five-Orbital Hubbard-Holstein Model, *Phys. Rev. Lett.* **104**, 157001 (2010).

[58] A. A. Tsirlin, P. Fertey, B. R. Ortiz, B. Klis, V. Merkl, M. Dressel, S. D. Wilson, and E. Uykur, Role of Sb in the superconducting kagome metal CsV_3Sb_5 revealed by its anisotropic compression, arXiv:2105.01397 (available at <https://arxiv.org/abs/2105.01397>).

[59] C. Mielke III, D. Das, J.-X. Yin, H. Liu, R. Gupta, C. N. Wang, Y.-X. Jiang, M. Medarde, X. Wu, H. C. Lei, J. J. Chang, P. Dai, Q. Si, H. Miao, R. Thomale, T. Neupert, Y. Shi, R. Khasanov, M. Z. Hasan, H. Luetkens, and Z. Guguchia, Time-reversal symmetry-breaking charge order in a correlated kagome superconductor, arXiv:2106.13443 (available at <https://arxiv.org/abs/2106.13443>).

[60] Q. Wu, Z. X. Wang, Q. M. Liu, R. S. Li, S. X. Xu, Q. W. Yin, C. S. Gong, Z. J. Tu, H. C. Lei, T. Dong, and N. L. Wang, The large static and pump-probe Kerr effect with two-fold rotation symmetry in Kagome metal CsV_3Sb_5 , arXiv:2110.11306 (available at <https://arxiv.org/abs/2110.11306>).

[61] C. M. Varma, Non-Fermi-liquid states and pairing instability of a general model of copper oxide metals, *Phys. Rev. B* **55**, 14554 (1997).

[62] I. Affleck and J. B. Marston, Large- n limit of the Heisenberg-Hubbard model: Implications for high- T_c superconductors, *Phys. Rev. B* **37**, 3774(R) (1988).

[63] H. Kontani, Y. Yamakawa, R. Tazai, and S. Onari, Odd-parity spin-loop-current order mediated by transverse spin fluctuations in cuprates and related electron systems, *Phys. Rev. Research* **3**, 013127 (2021).

[64] R. Tazai, Y. Yamakawa, and H. Kontani, Emergence of charge loop current in the geometrically frustrated Hubbard model: A functional renormalization group study, *Phys. Rev. B* **103**, L161112 (2021).

[65] S.-Y. Yang, Y. Wang, B. R. Ortiz, D. Liu, J. Gayles, E. Derunova, R. Gonzalez-Hernandez, L. Šmejkal, Y. Chen,

S. S. P. Parkin, S. D. Wilson, E. S. Toberer, T. McQueen, and M. N. Ali, Giant, unconventional anomalous Hall effect in the metallic frustrated magnet candidate, KV_3Sb_5 , *Sci. Adv.* **6**, eabb6003 (2020).

[66] F. H. Yu, T. Wu, Z. Y. Wang, B. Lei, W. Z. Zhuo, J. J. Ying, and X. H. Chen, Concurrence of anomalous Hall effect and charge density wave in a superconducting topological kagome metal, *Phys. Rev. B* **104**, L041103 (2021).

[67] Y. Gan, W. Xia, L. Zhang, K. Yang, X. Mi, A. Wang, Y. Chai, Y. Guo, X. Zhou, and M. He, Magneto-Seebeck effect and ambipolar Nernst effect in the CsV_3Sb_5 superconductor, *Phys. Rev. B* **104**, L180508 (2021).

[68] H. Kontani, Anomalous transport phenomena in Fermi liquids with strong magnetic fluctuations, *Rep. Prog. Phys.* **71**, 026501 (2008).

Acknowledgments

Funding: This study has been supported by Grants-in-Aid for Scientific Research from MEXT of Japan (JP18H01175, JP17K05543, JP20K03858, JP20K22328), and by the Quantum Liquid Crystal No. JP19H05825 KAKENHI on Innovative Areas from JSPS of Japan.

Author contributions: R.T. performed the all calculations discussing with Y.Y., S.O., and H.K., and R.T. and H.K. wrote the paper.

Competing interests: The authors declare that they have no competing interests.

Data and materials availability: All data needed to evaluate the conclusions in the paper are present in the paper and/or the Supplementary Materials.

[Supplementary Materials]

Mechanism of exotic density-wave and beyond-Migdal unconventional superconductivity in kagome metal AV_3Sb_5 ($\text{A}=\text{K, Rb, Cs}$)

Rina Tazai, Youichi Yamakawa, Seiichiro Onari, and Hiroshi Kontani

Department of Physics, Nagoya University, Nagoya 464-8602, Japan

A: Model Hamiltonian and RPA

In the main text, we analyze the kagome lattice model shown in Fig. 1 (b) introduced in Ref. [25]. In this model, a unit cell contains three sites (A, B, C), and each site possesses two orbitals (b_{3g} and b_{2g}). In the theoretical analysis, it is more convenient to study a completely equivalent “six-orbital triangular lattice model” in Fig. S1: It is derived from the kagome lattice model by shifting three apical sites (A, B, C) of each upper triangular to its center, without changing the hopping integrals and the Coulomb interaction terms. One of the great merits of analyzing this triangular model is that any inter-site vector $\mathbf{r}_i - \mathbf{r}_j$ is equal to a translation vector, and therefore functions in the momentum space (such as $\chi_{ll',mm'}^s(\mathbf{q})$ and $f_{\mathbf{q}}^{lm}(\mathbf{k})$) become periodic in the first Brillouin zone (BZ). For this reason, we perform the numerical study in the main text based on the triangular lattice model in Fig. S1.

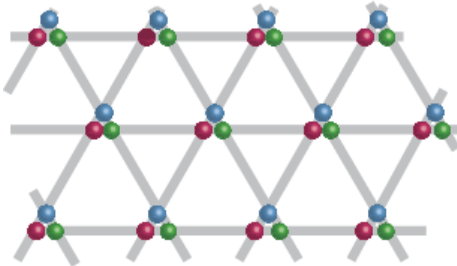


FIG. S1: Six-orbital triangular lattice model: In this model, three apical sites (A, B, C) of each upper triangular site in the kagome lattice are located at the same position. This model is convenient for the numerical study because both intra- and inter-orbital susceptibilities become periodic in the first BZ.

Next, we explain the multiorbital Coulomb interaction. The matrix expression of the spin-channel Coulomb interaction is

$$U_{l_1l_2,l_3l_4}^s = \begin{cases} U, & l_1 = l_2 = l_3 = l_4 \\ U', & l_1 = l_3 \neq l_2 = l_4 \\ J, & l_1 = l_2 \neq l_3 = l_4 \\ J', & l_1 = l_4 \neq l_2 = l_3 \end{cases} \quad (\text{S1})$$

in the case that $l_1 \sim l_4$ are orbitals (X, X') at site X ($=\text{A,B,C}$). In other cases, $U_{l_1l_2,l_3l_4}^s = 0$. Also, the matrix

expression of the charge-channel Coulomb interaction is

$$U_{l_1l_2,l_3l_4}^c = \begin{cases} -U, & l_1 = l_2 = l_3 = l_4 \\ U' - 2J, & l_1 = l_3 \neq l_2 = l_4 \\ -2U' + J, & l_1 = l_2 \neq l_3 = l_4 \\ -J', & l_1 = l_4 \neq l_2 = l_3 \end{cases} \quad (\text{S2})$$

in the case that $l_1 \sim l_4$ are orbitals (X, X') at site X ($=\text{A,B,C}$). In other cases, $U_{l_1l_2,l_3l_4}^c = 0$. Here, U (U') is the intra-orbital (inter-orbital) Coulomb interaction, J is the Hund’s coupling, and J' is the pair hopping term. In the main text, we assume the relations $U = U' + 2J$ and $J = J'$, and set the constraint $J/U = 0.10$. The obtained results are not sensitive to the ratio J/U .

The spin (charge) susceptibility in the RPA, $\chi_{ll',mm'}^{s(c)}(q)$, is given by

$$\hat{\chi}^{s(c)}(q) = \hat{\chi}^0(q)(\hat{1} - \hat{U}^{s(c)}\hat{\chi}^0(q))^{-1}, \quad (\text{S3})$$

where the element of the irreducible susceptibility is $\chi_{ll',mm'}^0(q) = -\frac{T}{N} \sum_k G_{lm}(k+q)G_{m'l'}(k)$. $G_{lm}(k)$ is the (l, m) element of the electron Green function: $\hat{G} = (\epsilon_n \hat{1} - \hat{H}_0(\mathbf{k}))^{-1}$.

In the present model, $\chi_{ll',mm'}^s(q)$ is small unless all orbitals belong to b_{3g} . Also, $\chi_{ll',mm'}^s(q)$ becomes large only when $l = l' = m = m'$ and $l = \text{A or B or C}$. The spin susceptibility in the present model is shown in Fig. 1 (e) in the main text.

B: Robustness of bond-order solution in the DW equation

In the main text, we present the numerical results for $n = 3.8$. In this case, the b_{3g} -orbital FS is very close to the vHS points on the BZ boundary as shown in Fig. 1 (d), consistently with recent ARPES reports. In this model, the van Hove filling is $n_{\text{vHS}} = 3.71$, and the single large FS around Γ point is divided into two pockets around K and K' points for $n < n_{\text{vHS}}$. Thus, it is important to verify the robustness of numerical results for different electron filling n .

First, we study the case of $n < 3.8$. Figures S2 (a) and (b) represent the FS at $n = 3.6$ and 3.7, respectively. The obtained eigenvalue of the DW equation at $n = 3.6$ and 3.7 in the case of $\alpha_S = 0.8$ is

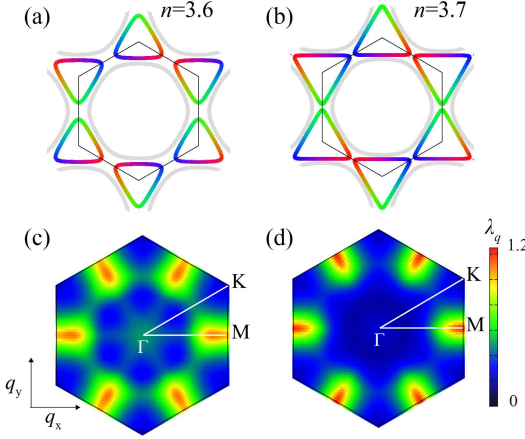


FIG. S2: **Robustness of bond-order solution:** (a) FS for $n = 3.6$ and (b) FS for $n = 3.7$. (c) \mathbf{q} -dependence of the eigenvalue for $n = 3.6$ (incommensurate) and (d) that for $n = 3.7$ (commensurate). Here, $U = 1.34$ (1.25) for $n = 3.6$ (3.7).

shown in Figs. S2 (c) and (d), respectively. Thus, the commensurate-incommensurate (C-IC) transition occurs between $n = 3.7$ and 3.6. In both cases, the smectic bond-order at \mathbf{q}_n ($n = 1, 2, 3$) is satisfactorily obtained, irrespective of the Lifshitz transition at $n_{\text{vHS}} = 3.71$. Therefore, we conclude that the strong electron correlation due to the three vHS points is essential for the formation of the bond-order, while the shape and the topology of FS are not essential. We stress that the second-largest eigenvalue is much smaller than the present bond-order eigenvalue at $\mathbf{q} = \mathbf{q}_1$.

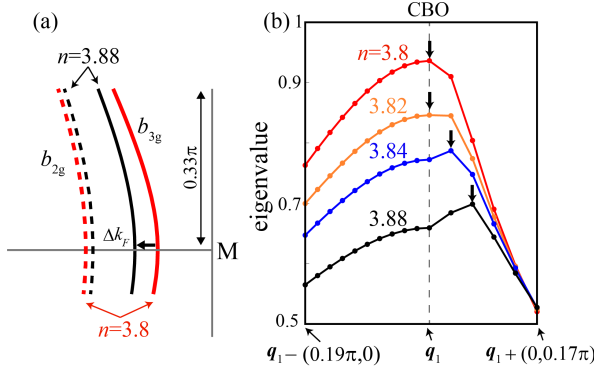


FIG. S3: **C-IC bond-order transition in the six orbital model:** (a) n -dependence of the FS in the six orbital model around M point. (The whole FS at $n = 3.8$ is shown in Fig. 1 (a).) The reduction in the b_{3g} -orbital Fermi momentum is expressed as Δk_F . Here, CBO means the commensurate bond-order. (b) Obtained \mathbf{q} -dependence of the eigenvalue for bond-order at $T = 0.01$ and $\alpha_S = 0.8$. The C-IC transition occurs at $n = n_0 \equiv 3.82$. The wavevector of the DW state is $\mathbf{q}_{\text{DW}} = \mathbf{q}_1 + (0, \delta)$, and $\delta > 0$ for $n > n_0$. Here, $U = 1.18$ (1.21) at $n = 3.80$ (3.88).

Next, we study the case of $n \geq 3.8$. Figures S3 (a) and (b) exhibits the FSs and the \mathbf{q} -dependence of the bond-order eigenvalue $\lambda_{\mathbf{q}}$, respectively, in the present simple six orbital model at $T = 0.01$. U is set to satisfy $\alpha_S = 0.80$ at each n . For $n \leq n_0 \equiv 3.82$, the wavevector of the bond-order is commensurate: $\mathbf{q}_{\text{DW}} = \mathbf{q}_1 \equiv (\frac{2}{\sqrt{3}}\pi, 0)$. For $n > n_0$, it changes to incommensurate at $\mathbf{q}_{\text{DW}} = \mathbf{q}_1 + (0, \delta)$. The realized electron-doping in the b_{3g} -orbital FS is $\Delta n_{b_{3g}} = 0.7(n - n_0)$. The induced shift of the b_{3g} -orbital Fermi momentum on the k_x -axis is $\Delta k_F = -0.62\pi \times \Delta n_{b_{3g}}$. Thus, $\Delta k_F = -0.02\pi$ is realized when $\Delta n_{b_{3g}} = 0.033$ (or $n = n_0 + 0.046$). On the other hand, in the realistic 30 orbital model in SM G, $\Delta k_F = -0.02\pi$ is induced by the self-doping ($\sim 1.5\%$) at $P = 3\text{GPa}$. Thus, the C-IC bond-order transition can also be understood based on the present simple six orbital Hubbard model.

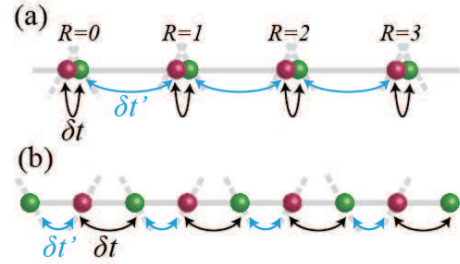


FIG. S4: **Origin of bond-order solution in kagome metal:** (a) Nearest-neighbor hopping modulations δt and $\delta t'$ under the bond-order at $\mathbf{q} = \mathbf{q}_3$ in the triangular lattice model in Fig. S1. (b) δt and $\delta t'$ in the kagome lattice model in Fig. 1 (b).

These numerical results indicates the importance of the vHS points. Hereafter, we discuss a simplified DW equation by focusing on the vHS points in order to understand why bond-order is obtained. For the bond-order at $\mathbf{q} = \mathbf{q}_3$, only vHS points A and C are essential, so we consider a simple two-component form factor $(f_1, f_2) \equiv (f_{\mathbf{q}_3}^{CA}(\mathbf{k}_A), f_{\mathbf{q}_3}^{AC}(\mathbf{k}_C))$. Then, the DW equation at $\mathbf{q} = \mathbf{q}_3$ is given as

$$\lambda \begin{pmatrix} f_1 \\ f_2 \end{pmatrix} \sim N(0) \begin{pmatrix} g_{\text{back}} & g_{\text{um}} \\ g_{\text{um}} & g_{\text{back}} \end{pmatrix} \begin{pmatrix} f_1 \\ f_2 \end{pmatrix}, \quad (\text{S4})$$

where $N(0)$ is the density-of-states at the Fermi level. As we explain in the main text, both g_{back} and g_{um} are positive. Thus, the largest eigenvalue and the eigenvector are $\lambda \sim N(0)(g_{\text{back}} + g_{\text{um}})$ and $\mathbf{f} = (1, 1)$, respectively. After the Fourier transformation, the real-space form factor in the triangular lattice model in Fig. S1 is given as $\delta t_{CA}(R\mathbf{e}_{\perp}) \sim f_{CA}(\mathbf{k}_A)e^{i\pi R}$ and $\delta t_{AC}(R\mathbf{e}_{\perp}) \sim f_{AC}(\mathbf{k}_C)e^{i\pi R}$. Here, R is an integer, and \mathbf{e}_{\perp} is a unit vector perpendicular to \mathbf{q}_3 . By making comparison between Fig. S1 and Fig. 1 (b) in the main text, the nearest-neighbor hopping modulations in Fig. S4 (a) are given as $(\delta t, \delta t') = (\delta t_{CA}(\mathbf{0}), \delta t_{AC}(\mathbf{e}_{\perp})) \propto (1, -1)$.

The same bond-order in the kagome lattice model is shown in Fig. S4 (b). When $\delta t = -\delta t'$, it is equivalent to Fig. 2 (d) in the main text. Therefore, the essential origin of the bond-order is naturally understood based on a simple two vHS model in Eq. (S4).

C: Unfolded Fermi surface under triple- \mathbf{q} state

In the triple- \mathbf{q} DW state, both the FS and the band-structure are folded into the folded BZ. They can be unfolded into the original size BZ, which correspond to the ARPES measurement in the DW state. The obtained unfolded FS in the case of $\max_{\mathbf{k}} \{f_{\mathbf{q}_n}(\mathbf{k})\} = 0.018$ [eV] is shown in Fig. S5. Here, the spectra around the vHS points are gapped. This result is consistent with the recent ARPES studies.

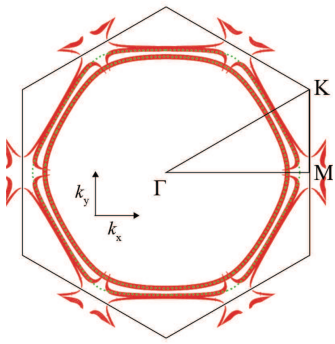


FIG. S5: **Unfolded FS under the triple- \mathbf{q} bond-order:** The FS near the vHS points is reconstructed by the bond-order. The result for $\max_{\mathbf{k}} \{f_{\mathbf{q}_n}(\mathbf{k})\} = 0.018$ [eV] is shown. The green dotted lines represent the original FS.

D: GL free energy in D_{6h} kagome model

Here, we briefly review the GL free energy of a D_{6h} system up to the fourth order and explain that the triple- \mathbf{q} order is stabilized by the third-order term. We introduce three real order parameters ϕ_n ($n = 1 - 3$) and express the bond-order functions as $\phi_n \hat{f}_{\mathbf{q}_n}(\mathbf{k})$, where $\hat{f}_{\mathbf{q}_n}(\mathbf{k})$ is the normalized dimensionless form factor given by the linearized DW equation. [Note that the phase factor of the form factor is fixed by the Hermite condition $f_q^{lm}(k) = [f_{-q}^{im}(k + q)]^*$.] The GL free energy is given as [48]

$$F = a[\phi_1^2 + \phi_2^2 + \phi_3^2] + b\phi_1\phi_2\phi_3 + c[\phi_1^4 + \phi_2^4 + \phi_3^4] + d[\phi_1^2\phi_2^2 + \phi_2^2\phi_3^2 + \phi_3^2\phi_1^2] \quad (\text{S5})$$

where the second-order coefficient a is proportional to $1 - \lambda_{\text{bond}}$. The fourth-order coefficients c, d are positive. Here, the third-order coefficient b is nonzero because of

the momentum conservation relation $\mathbf{q}_1 + \mathbf{q}_2 + \mathbf{q}_3 = \mathbf{0}$. Note that the sign of b is reversed under the transformation $f \rightarrow -f$.

One can calculate the coefficients b , c , and d microscopically based on their diagrammatic expressions given in our previous paper on 1T-TaS₂ [48]: The coefficient b is given by the triangle diagram composed of three Green functions and three form factors. In a similar way, the coefficients c and d are given by the square diagrams.

Based on the GL free energy, the single- \mathbf{q} solution $(\phi_1, \phi_2, \phi_3) = (\phi, 0, 0)$ occurs when $a \leq 0$ as the second-order transition. On the other hand, in the case of the triple- \mathbf{q} order, the free energy is $F(\phi) = a\phi^2 + b\phi^3/3\sqrt{3} + (c + d)\phi^4/3$. In the case $a > 0$, its local minimum is given at $\phi_0 = \frac{-\sqrt{3}b}{8(c+d)} \left(1 - \sqrt{1 - \frac{32a}{b^2}(c+d)} \right)$, which is positive [negative] for $b < 0$ [$b > 0$]. The free energy $F(\phi_0)$ becomes negative when $a < b^2/[36(c+d)]$ (=positive). Therefore, triple- \mathbf{q} order is realized as the first order transition when a is positive. (That is, ϕ jumps from zero to ϕ_0 at finite $a > 0$.) Consistently with this analysis, the star of David bond-order emerges as a weak first order transition experimentally.

E: Derivation of SC gap equation

Here, we discuss the reason why bond-order fluctuations mediate the pairing interaction. In Ref. [5], the authors studied the orbital fluctuation mediated *s*-wave superconductivity in Fe-based superconductors. In that study, the electron-boson coupling (=form factor) is an orbital-dependent but \mathbf{k} -independent charge quadrupole operator: $\hat{f}^{\mathbf{q}}(\mathbf{k}) = \hat{O}_{\Gamma}$ ($\Gamma = xz, yz, xy$). In the main text, we obtain the development of bond-order fluctuations with the \mathbf{k} -dependent form factor in AV₃Sb₅, which is given by the inter-sublattice vertex corrections (VCs) that are dropped in the RPA. We reveal that bond-order fluctuations mediate significant “beyond-Migdal” pairing interaction thanks to the \mathbf{k} -dependent form factor [44], and therefore *s*-wave and *p*-wave SC states emerge in AV₃Sb₅.

In the following, we discuss the pairing interaction due to the bond-order fluctuations in kagome metal by following Ref. [44]. Hereafter, we drop the orbital indices just to simplify the notation. The pairing interaction between Cooper pairs $(k, -k)$ and $(k', -k')$ due to charge-channel full four-point vertex in Fig. 7 (c) is given as $V(k, k') \propto \Gamma_{k'-k}^c(k, -k')$. We derive a convenient simple expression of $\Gamma_{\mathbf{q}}^c(k, k')$, we introduce the following approximation for the kernel function:

$$I_{\mathbf{q}}(\mathbf{k}, \mathbf{k}') = \bar{I}_{\mathbf{q}} f_{\mathbf{q}}(k) f_{\mathbf{q}}^*(k'), \quad (\text{S6})$$

where $f_{\mathbf{q}}(k)$ is the form factor for the largest eigenvalue of the DW equation. By inserting Eq. (S6) into the DW

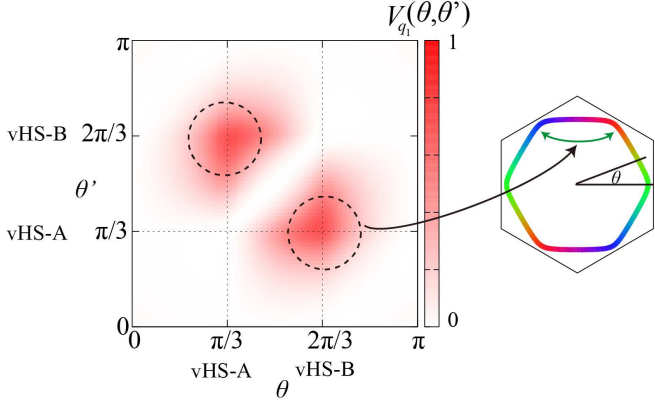


FIG. S6: **Pairing interaction on b_{3g} -orbital FS due to bond-order fluctuations:** We present $V_1(\theta, \theta')$ due to $\mathbf{q} \approx \mathbf{q}_1$ given in (S10) in the case of $\bar{I}_{\mathbf{q}} = 1$ and $\lambda_{\text{bond}} = 0$. Here, $\theta = \arctan(k_y/k_x)$ and $\theta' = \arctan(k'_y/k'_x)$.

equation, the eigenvalue is given as $\lambda_{\mathbf{q}} = \bar{I}_{\mathbf{q}} \chi_f^0(\mathbf{q})$, where

$$\chi_f^0(\mathbf{q}) = -\frac{T}{N} \sum_k G(k + \mathbf{q}) G(k) \tilde{f}_{\mathbf{q}}(k) \tilde{f}_{\mathbf{q}}^*(k). \quad (> 0) \quad (\text{S7})$$

Then, the full four-point vertex is given as

$$\Gamma_{\mathbf{q}}^c(k, k') = \frac{\bar{I}_{\mathbf{q}} f_{\mathbf{q}}(k) f_{\mathbf{q}}^*(k')}{1 - \lambda_{\mathbf{q}}}. \quad (\text{S8})$$

Therefore, the pairing interaction is $V(k, k') = \frac{\bar{I}_{\mathbf{q}} f_{\mathbf{q}}(k) f_{\mathbf{q}}^*(-k')}{1 - \lambda_{\mathbf{q}}}$, where $\mathbf{q} = \mathbf{k}' - \mathbf{k}$. Note that the relation $f_{\mathbf{q}}^*(-k') = f_{-\mathbf{q}}(-k)$ holds for $\mathbf{q} = \mathbf{k}' - \mathbf{k}$ due to the Hermite condition of the form factor.

Considering that the \mathbf{q} -dependence of the form factor is moderate, the total pairing interaction due to triple- \mathbf{q} bond-order fluctuations is approximately given as

$$V_{\text{bond}}(k, k') = \frac{1}{2} \sum_n^{1,2,3} V_n(k, k'), \quad (\text{S9})$$

$$\begin{aligned} V_n(k, k') &= \frac{\bar{I}_{\mathbf{q}} \bar{f}_{\mathbf{q}_n}(\mathbf{k}) \bar{f}_{\mathbf{q}_n}^*(-\mathbf{k}')}{1 - \lambda_{\mathbf{k}' - \mathbf{k}}} \\ &\approx \frac{\bar{I}_{\text{bond}} \bar{f}_{\mathbf{q}_n}(\mathbf{k}) \bar{f}_{-\mathbf{q}_n}(-\mathbf{k})}{1 - \lambda_{\text{bond}}} \frac{1}{1 + \xi^2(\mathbf{q}_n - (\mathbf{k}' - \mathbf{k}))^2}, \end{aligned} \quad (\text{S10})$$

where $\bar{f}^{\mathbf{q}}(\mathbf{k}) \equiv \sum_{l,m} \tilde{f}_{lm}^{\mathbf{q}}(\mathbf{k}) u_{l,b}(\mathbf{k} + \mathbf{q})^* u_{m,b}(\mathbf{k})$. Here, $u_{l,b}(\mathbf{k}) = \langle l, \mathbf{k} | b, \mathbf{k} \rangle$ is the unitary transformation matrix element between orbital l and conduction band b , and $\bar{f}^{\mathbf{q}}(\mathbf{k}) \equiv (f^{\mathbf{q}}(\mathbf{k}, \pi T) + f^{\mathbf{q}}(\mathbf{k}, -\pi T))/2$. We also approximate $\lambda_{\mathbf{q}} \approx \lambda_{\text{bond}} - b(\mathbf{q} - \mathbf{q}_n)^2$ with $b \approx \xi^2(1 - \lambda_{\text{bond}})$ for $\mathbf{q} \sim \mathbf{q}_n$. Here, we set $\bar{f}_{\mathbf{q}_1}^{BA}(k_B) = 1$. Then, the coupling constant \bar{I}_{bond} is directly given by g_{um} that is obtained in the main text. We stress that $\bar{f}_{\mathbf{q}_n}(k) \bar{f}_{-\mathbf{q}_n}(-k)$ is positive for even-parity bond-order. In the main text, we set

$\bar{I}_{\text{bond}} = g_{\text{um}} |\bar{f}_{\mathbf{q}_1}(\mathbf{k}_A)| = 1$ in the pairing interaction in Eq. (S10).

Figure S6 is the pairing interaction $V_1(\theta, \theta')$ on the b_{3g} -orbital FS due to the bond-order fluctuations at wavevector $\mathbf{q} \approx \mathbf{q}_1$ by setting $\bar{I}_{\mathbf{q}} = 1$, $\lambda_{\text{bond}} = 0$ and $\xi = 0$. Here, $\theta = \arctan(k_y/k_x)$ and $\theta' = \arctan(k'_y/k'_x)$. Thus, strong attractive pairing interaction is induced by the bond-order fluctuations around the vHS points. This is the driving force of the s -wave and p -wave pairing states obtained in the main text.

In the main text, we solve the gap equation in the presence of bond and spin fluctuations.

$$V_s^{\text{SC}}(k, k') = V_{\text{bond}}(k, k') - \frac{3}{2} U^2 \chi^s(k - k') - U, \quad (\text{S11})$$

$$V_t^{\text{SC}}(k, k') = V_{\text{bond}}(k, k') + \frac{1}{2} U^2 \chi^t(k - k'), \quad (\text{S12})$$

where s (t) represents the singlet (triplet) pairing interaction. The diagrammatic expression of the gap equation due to $V_{\text{bond}}(k, k')$ is depicted in Fig. 4 (a) in the main text. In solving the gap equation, we set the BCS cutoff energy ω_c for V_{bond} because the energy-scale of bond-order fluctuations is much smaller than E_F . Here, we set $\omega_c = 0.02$. Note that the pairing interaction for the band b, b' can be derived from that in the orbital representation by using the unitary transformation matrix $u_{l,b}(\mathbf{k})$.

It is noteworthy that the present bond-order fluctuating pairing mechanism is outside of the Migdal approximation, in which the form factor is assumed to be \mathbf{k} -independent. The present bond-order fluctuating mechanism has a close similarity to the multiple-fluctuation pairing mechanism developed in Refs. [43, 44].

F: Comparison between the present DW equation theory and mean-field theory

A great merit of the present paramagnon-interference theory is that the star of David bond-order is naturally obtained based on a simple Hubbard model without introducing any off-site Coulomb interactions. Here, we briefly review the results of the mean-field theory based on the U - V Hubbard model, where V is the nearest-neighbor Coulomb interaction. For this purpose, we solve the linearized mean-field equation with the optimized form factor, which is given by Eq. (2) with the Hartree-Fock kernel function made of U and V . Figure S7 (a) shows the obtained eigenvalues as a function of V/U at $U = 0.79$. (Here, we drop b_{2g} orbitals in the kagome metal Hubbard model introduced in the main text, because b_{2g} orbitals are not essential for the bond-order.) The spin-density-wave (SDW) instability (with spin form factor $f^s = 1$) is the largest for $V \lesssim 0.4U$. The SDW is replaced with the spin-bond-order (spin-BO), $f^s \neq 1$ for $0.4U \lesssim V \lesssim 0.6U$, and the charge-density-wave (CDW) instability (with charge form factor $f^c = 1$) is the largest

for $V \gtrsim 0.6U$. Figure S7 (b) shows the results as functions of U/V at $V = 0.32$. Thus, the charge bond-order (charge-BO) instability is secondary in both Figs. S7 (a) and (b).

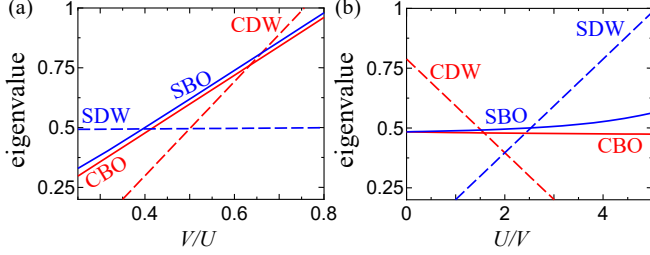


FIG. S7: **Mean-field analysis for U - V Hubbard model**: (a) Eigenvalues of the mean-field density-wave equation as a function of V/U at $U = 0.79$, and (b) those as a function of U/V at $V = 0.32$. Here, the charge-BO instability is smaller than other instabilities.

In contrast, the charge bond-order instability is solely magnified in the DW equation with MT and AL terms even for $V = 0$. Figure S8 exhibits the spin-channel and charge-channel eigenvalues, λ_q^s and λ_q^c , in the DW equation at $\mathbf{q} = \mathbf{0}$ and $\mathbf{q} = \mathbf{q}_1$ [63]. We see that $\lambda_{\mathbf{q}=\mathbf{q}_1}^c$, which is equivalent to λ_{bond} in the main text, solely increases with increasing $\alpha_S (\propto U)$. Thus, the bond-order solution is obtained for wide parameter range. Interestingly, $\lambda_{\mathbf{q}=\mathbf{0},\text{bond}} \equiv \lambda_{\mathbf{q}=\mathbf{0}}^c$, which corresponds to A_{1g} bond-order with sign-reversing form factor, starts to develop for $\alpha_S \gtrsim 0.8$.

By solving the spin-channel DW equation [63], we reveal that the spin channel eigenvalue $\lambda_{\text{spin}} \equiv \max_{\mathbf{q}} \lambda_{\mathbf{q}}^s$ is smaller than α_S only slightly, and it corresponds to the SDW solution with $f^s \approx 1$. (Note that $\lambda_{\text{spin}} = \alpha_S$ in the mean-field approximation for $V = 0$.) We stress that the spin-BO ($f^s \neq 1$) instability is always smaller than the SDW instability. In the present theory, the charge-channel AL term is proportional to the convolution $C^c(\mathbf{q}_1) = \sum_{\mathbf{k}} \chi^s(\mathbf{k} + \mathbf{q}_1) \chi^s(\mathbf{k})$, while the spin-channel one is proportional to $C^s(\mathbf{q}_1) = \sum_{\mathbf{k}} \chi^s(\mathbf{k} + \mathbf{q}_1) \chi^c(\mathbf{k})$, as we discussed in Refs. [9, 63]. Since $C^c(\mathbf{q}_1) \gg |C^s(\mathbf{q}_1)|$ for $\alpha_S \gtrsim 0.75$, only the charge bond-order eigenvalue λ_{bond} is strongly enlarged and exceeds unity in Fig. S8. Thus, the instability of the smectic bond-order is robust in kagome metals, while any spin-channel eigenvalues are smaller than unity even if the quantum interference mechanism is taken into account. This is a great merit of the present DW equation analysis.

G: Realistic model Hamiltonian based on the first-principles study

Based on the first-principles study, we derive the two-dimensional realistic model for CsV_3Sb_5 , which we analyzed in the main text. First, we perform the Wien2k

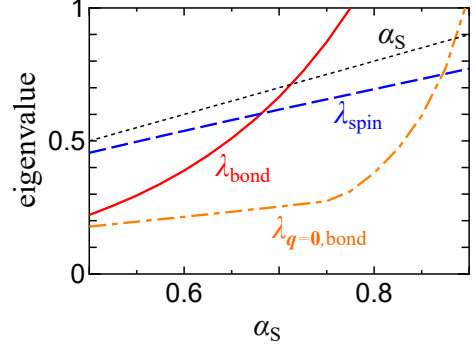


FIG. S8: **DW equation analysis for U Hubbard model**: Eigenvalue of DW equation with MT and AL terms as a function of $\alpha_S (\propto U)$. Here, the eigenvalue of charge-channel bond-order $\lambda_{\text{bond}} \equiv \lambda_{\mathbf{q}_1}^c$ solely increases due to the AL terms. In contrast, the spin-channel eigenvalue $\lambda_{\text{spin}} \equiv \lambda_{\mathbf{q}_1}^s$ remains small even if the spin-channel vertex corrections are taken into account. Interestingly, $\lambda_{\mathbf{q}=\mathbf{0},\text{bond}} \equiv \lambda_{\mathbf{q}=\mathbf{0}}^c$, which corresponds to A_{1g} bond-order with sign-reversing form factor, starts to develop for $\alpha_S \gtrsim 0.8$.

DFT calculation of CsV_3Sb_5 under pressure P [GPa], using the crystal structure data in Ref. [58]. Next, we derive the 30 orbital (15 3d-orbitals + 15 5p-orbitals) tight-binding model, $H_0^{\text{DFT}}(P)$, using the Wannier90 software. The DFT band dispersions are fitted almost perfectly. Here, we drop the inter-layer hopping integrals. The bandstructure along the k_x -axis at $P = 0$ is shown in Fig. S9 (a). The green line is the b_{3g} -orbital band, and its width represents the b_{3g} -orbital weight. The bandstructure in Fig. S9 (a) is qualitatively similar to ARPES data. However, Fig. S9 (a) is different from the experimental CsV_3Sb_5 bandstructure [31, 53, 54] at the following two points: (i) The vHS energy E_{vHS} is not adjacent to the Fermi level E_F . (ii) The b_{3g} -band crosses a 5p-band around M point, so the b_{3g} -orbital weight disappears via the band hybridization except on the k_x -axis.

We will fix these discrepancies by introducing *minimum changes* in the Hamiltonian. Here, we shift 15 5p-orbital levels by $\Delta E_p = -0.2$ [eV] and introduce the hole-doping by 0.1 to make E_{vHS} closer to E_F . (The orbital-dependent energy shift method is frequently applied in Fe-based superconductors to reproduce experimental FSs [9].) The obtained modified bandstructure is shown in Fig. S9 (b) and its FS is presented in Fig. 6 (a), which are consistent with recent STM and ARPES measurements [31, 53, 54]. We use this model as the model Hamiltonian at ambient pressure, $H_0(P = 0)$.

Next, we discuss the pressure dependence of the Hamiltonian caused by the systematic change in the crystal structure. It is described by the ‘‘pressure Hamiltonian $\Delta H_0^{\text{DFT}}(P) \equiv H_0^{\text{DFT}}(P) - H_0^{\text{DFT}}(0)$ ’’. Then, the model Hamiltonian is given as

$$H_0(P) = H_0(0) + \Delta H_0^{\text{DFT}}(P). \quad (\text{S13})$$

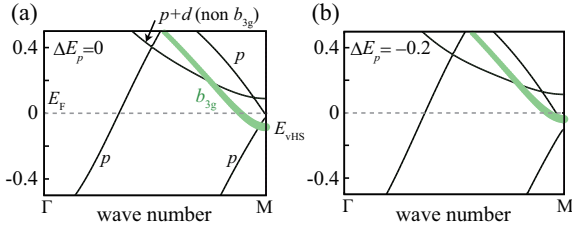


FIG. S9: **Band structure based on the first-principles calculation:** (a) Original DFT band structure for CsV_3Sb_5 in the case of $\Delta E_p = 0$. (b) Modified band structure with $\Delta E_p = -0.2$ and 0.1 hole-doping.

This method has been successfully applied to the study of P - T phase diagram in Fe-based superconductors. The obtained FSs at $P = 0$ and 3GPa are shown in Figs. 6 (a) and (b). Under pressure, the volume of b_{3g} -orbital FS is reduced because the b_{3g} -orbital level shifts downward relatively. The self-doping on the b_{3g} -FS ($\sim 1.5\%$ at $P = 3\text{GPa}$) derived from $\Delta H_0^{\text{DFT}}(P)$ will be reliable. At the same time, the bandwidth increases under pressure, and the spin Stoner factor α_S is reduced by 0.03 at $P = 3\text{GPa}$. (In this model, $\alpha_S = 0.95$ at $U = 2.7$ [eV] when $P = 0$.) By using Eq. (S13), the pressure-induced C-IC bond-order transition is explained in the main text. It is an important future problem to analyze three-dimensional Hubbard model of CsV_3Sb_5 .

- [1] X. Wu, T. Schwemmer, T. Muller, A. Consiglio, G. Sangiovanni, D. Di Sante, Y. Iqbal, W. Hanke, A. P. Schnyder, M. M. Denner, M. H. Fischer, T. Neupert, and R. Thomale, arXiv:2104.05671.
- [2] S. Onari, Y. Yamakawa, and H. Kontani, Phys. Rev. Lett. **116**, 227001 (2016).
- [3] S. Onari and H. Kontani, Phys. Rev. Research **2**, 042005(R) (2020); S. Onari and H. Kontani, Phys. Rev. B **100**, 020507(R) (2019).
- [4] S. Onari and H. Kontani, Phys. Rev. Lett. **109**, 137001 (2012).
- [5] K. Kawaguchi, Y. Yamakawa, M. Tsuchiizu, and H. Kontani, J. Phys. Soc. Jpn. **86**, 063707 (2017).
- [6] Y. Yamakawa, S. Onari, and H. Kontani, Phys. Rev. X **6**, 021032 (2016).
- [7] R. Tazai, Y. Yamakawa, M. Tsuchiizu, and H. Kontani, arXiv:2105.01872.
- [8] R. Tazai and H. Kontani, Phys. Rev. B **100**, 241103(R) (2019).
- [9] M. Tsuchiizu, K. Kawaguchi, Y. Yamakawa, and H. Kontani, Phys. Rev. B **97**, 165131 (2018).
- [10] R. Tazai, Y. Yamakawa, M. Tsuchiizu, and H. Kontani, Phys. Rev. Research **3**, L022014 (2021).
- [11] H. Kontani, T. Saito, and S. Onari, Phys. Rev. B **84**, 024528 (2011).
- [12] R. Tazai and H. Kontani, Phys. Rev. B **98**, 205107 (2018).

This figure "fig2.png" is available in "png" format from:

<http://arxiv.org/ps/2107.05372v4>